



AKADÉMIAI KIADÓ

Central European
Geology

64 (2021) 2, 91–112

DOI:
[10.1556/24.2021.00004](https://doi.org/10.1556/24.2021.00004)
© 2021 The Author(s)

ORIGINAL RESEARCH
PAPER



Contrasting metamorphic and post-metamorphic evolutions within the Algyó basement high (Tisza Mega-unit, SE Hungary). Consequences for structural history

HENRIETTA KONDOR*  and TIVADAR M. TÓTH

Department of Mineralogy, Geochemistry and Petrology, University of Szeged, Szeged, Hungary

Received: July 2, 2020 • Accepted: September 18, 2020
Published online: April 26, 2021

ABSTRACT

The Algyó High (AH) is an elevated crystalline block in southeastern Hungary covered by thick Neogene sediments. Although productive hydrocarbon reservoirs are found in these Neogene sequences, numerous fractured reservoirs also occur in the pre-Neogene basement of the Pannonian Basin. Based on these analogies, the rock body of the AH might also play a key role in fluid storage and migration; however, its structure and therefore the reservoir potential is little known. Based on a comprehensive petrologic study in conjunction with analysis of the spatial position of the major lithologies, the AH is considered to have been assembled from blocks with different petrographic features and metamorphic history. The most common lithologies of garnet-kyanite gneiss and mica schist associated with garnetiferous amphibolite are dominant in the northwestern and southeastern parts of the AH. The first regional amphibolite facies metamorphism of the gneiss and mica schist was overprinted by a contact metamorphic (metasomatic) event during decompression in the stability field of kyanite. Garnet-bearing amphibolite experienced amphibolite facies peak conditions comparable with the host gneiss. Regarding the similarities in petrologic features, the northwestern and southeastern parts of the area represent disaggregated blocks of the same rock body. The central part of the AH area is characterized by an epidote gneiss-dominated block metamorphosed along with a greenschist-facies retrograde pathway as well as a chlorite schist-dominated block formed by greenschist-facies progressive metamorphism. The independent evolution of these two blocks is further confirmed by the presence of a propylitic overprint in the chlorite schists. The different metamorphic blocks of the northwestern, southeastern and central parts of the AH probably became juxtaposed along post-metamorphic normal faults developed due to extensional processes. The supposed brittle structural boundaries between the blocks could have provided hydrocarbon migration pathways from the adjacent over-pressured sub-basins, or could even represent suitable reservoirs.

KEYWORDS

Pannonian Basin, Algyó High, petrology, metamorphic evolution, structural history

INTRODUCTION

The basement of the Pannonian Basin consists of a complicated mosaic of structural blocks assembled during its Mesozoic-Neogene multistage tectonic evolution. During the Neogene, the basement was buried by the influx of Neogene sediments prevalent within the entire Pannonian Basin. Although the most productive hydrocarbon reservoirs are found in these Neogene sequences, hydrocarbon reservoirs do not only exist in these sediments. For instance, the basement may also act as a fractured groundwater or hydrocarbon reservoir, where brittle fault zones play an important role in fluid storage and migration.

One of the most essential hydrocarbon fields of the Pannonian Basin is situated in the southeastern part of Hungary. Within the local petroleum system (Dolton, 2006), the major

*Corresponding author. Department of Mineralogy, Geochemistry and Petrology, University of Szeged, Egyetem st. 2, H-6722 Szeged, Hungary.
E-mail: kondor.henrietta@gmail.com

source rocks of hydrocarbons are the Miocene marls and carbonates. Although the Paleogene and Neogene formations covering the basement highs have the best reservoir characteristics in the area, the Paleozoic crystalline basement not only participates in the migration but also the accumulation of hydrocarbons (Dolton, 2006; Babinszki and Kovács, 2018). Over the last few decades, numerous fractured, crystalline basement hydrocarbon reservoirs have been discovered in multiple locations around the basin, e.g., Dorozsma, Szeghalom, Mezősas-Furta or Kiskunhalas (M Tóth, 2008; M Tóth and Vargáne Tóth, 2020; Molnár et al., 2015; Nagy et al., 2013; Schubert et al., 2007).

The metamorphic Algyó High (AH) is located in the central region of the petroleum system of the area. Hydrocarbons migrated primarily from the adjacent over-pressured deep Neogene basins along the weathered slope of the basement forming several traps above the top of the dome in Neogene sandstones (Babinszki and Kovács, 2018). Based on several analogies, the rock body of the AH might also have played a key role in fluid storage and migration; however, only a few papers have been published about its structure and metamorphic history.

Recognition of petrographic features and structure of the AH is essential for a better understanding of its role within the petroleum system. The present study aims to characterize and classify the basement rocks and outline the spatial relationship of the major metamorphic lithologies. Mineralogical and geochemical analyses in conjunction with other spatial and *P-T* information are vital sources in establishing the geologic evolution of the basement.

GEOLOGIC SETTING

Within the Alpine-Carpathian-Dinaric orogenic belt, the Pannonian Basin consists of two different tectonic mega-units with different geologic histories, referred to as the Tisza-Dacia and ALCAPA Mega-units (Haas, 2001). During the Neogene, large-scale strike-slip movements led to the juxtaposition of these two microplates (Csontos et al., 1992; Fodor et al., 1999; Csontos and Vörös, 2004) (Fig. 1a).

The pre-Neogene basement of Pannonian Basin forms a complicated mosaic of structural blocks because of its multistage tectonic evolution. The metamorphic basement of the Tisza-Dacia Mega-unit is mainly comprised of Variscan metamorphic rocks with different metamorphic histories. The Variscan tectonic events were followed by a Cretaceous compressional phase, involving large-scale tectonic deformation resulting in a complicated nappe system throughout the pre-Neogene basement of the Pannonian Basin (Haas, 2001). Presently, the Tisza-Dacia Mega-unit includes four NW-facing nappes, in the following upward stratigraphic succession: Mecsek, Bihar, Codru and Biharja Nappe Systems (Fig. 1b) (Schmid et al., 2008). The Middle Miocene syn-rift extension caused the development of numerous low-angle normal fault systems, resulting in asymmetric half-graben structures and the exposure of metamorphic core complexes through uplift and exhumation of the crystalline cores (Tari et al., 1992; Tari, 1996). This regional event was followed by a tectonic inversion during the post-rift thermal sag phase, leading to spatial shortening and the reactivation of normal faults that continues today (Tari et al., 1999). As a

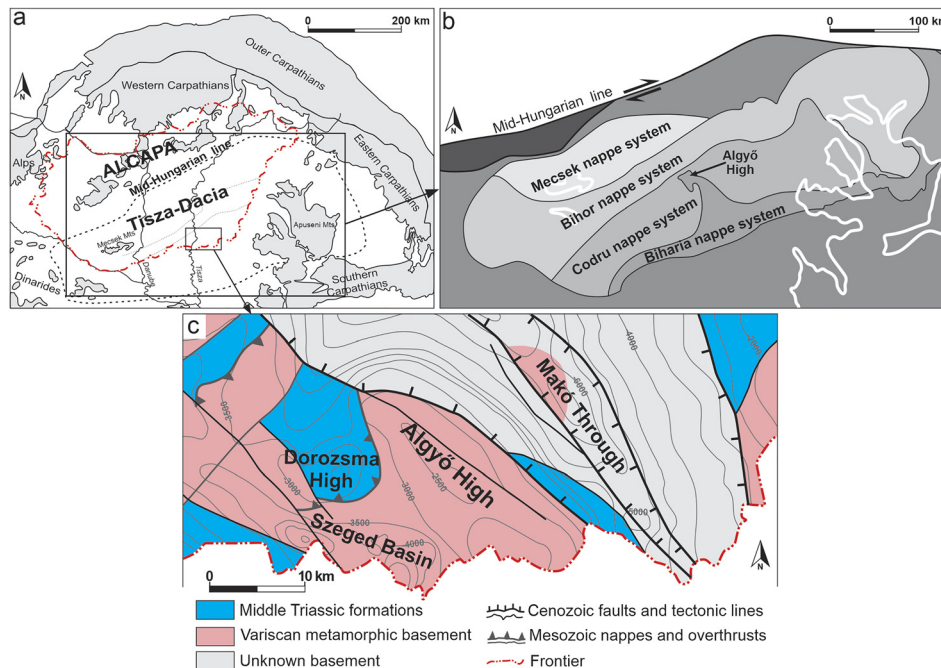


Fig. 1. Geologic and structural maps of the studied area: (a) location of Pannonian Basin within the Alpine-Carpathian belt (simplified after Csontos et al., 1992); (b) tectonic position of the AH within the Cretaceous nappe systems of Tisza-Dacia Mega-unit (modified after Schmid et al., 2008); (c) generalized pre-Cenozoic basement map of the studied area (modified after Haas et al., 2010)

result of widespread subsidence, sediments were gradually deposited in the entire Pannonian Basin, burying the remaining structural highs and filling the deep sub-basins (Horváth and Tari, 1999).

The AH is an elevated metamorphic narrow ridge at ~3,000 m below the present surface with a NW/SE orientation in the southeastern part of Hungary (Fig. 1). To the west of the crystalline complex lies the Szeged Basin, whereas the Makó Trough is found to the east, which is delineated by Miocene normal faults (Fig. 1c). Based on most interpretations, the metamorphic mass of the AH is considered to be part of the Tisza-Dacia Mega-unit. However, its position inside the Cretaceous nappe systems is rather controversial. According to some authors (Dimitrescu, 1995; Schmid et al., 2008; Matenco and Radivojevic, 2012), the AH belongs to the Biharia Nappe (Fig. 1b), yet others (Szederkényi, 1984; Horváth and Árkai, 2002) suggested that the AH can be classified into the Codru Nappe System. Based on the recent interpretation of Schmid et al. (2019), the AH is part of the Bihar Autochthonous Domain and is exposed in a tectonic window within the Codru Nappe System.

Limited contradictory information is available regarding the petrological character, metamorphic evolution and structural development of the AH. Based on some previous work, it is petrographically complex and includes different gneiss and mica schist varieties, amphibolite, chlorite schist and epidote-bearing rocks (T. Kovács and Kurucz, 1984; Szederkényi, 1984). T. Kovács and Kurucz (1984) suggested that these rock types correspond to locally distinct blocks and proposed structural boundaries between the neighboring blocks without any interpretation. Blocks dominated by gneiss and mica schist are typically found at the northern and southern portions of the area, whereas blocks of chlorite schists and epidote-bearing rocks are characteristic of the central region. In gneisses and mica schists, Lelkes-Felvári et al. (2003, 2005) and Szederkényi (1984) assumed the presence of pre-kinematic andalusite replaced by late kyanite based on the pseudomorphic shape of some kyanite aggregates; however, the presence of andalusite grains has yet to be documented, and this theory is also not supported by thermobarometric data.

Horváth and Árkai (2002) studied garnet-kyanite-bearing and garnet-sillimanite-bearing gneisses and mica schists from the southern part of the AH. By comparing the chemical composition and the zoning profile of the garnet grains, two progressive metamorphic events can be distinguished for the kyanite-bearing samples. The first event can be characterized by temperatures and pressures of 520–560 °C and 820–1,010 MPa in the presence of staurolite, whereas the second event yielded peak metamorphic conditions at 570–650 °C and 600–900 MPa. Decomposition of staurolite and the presence of garnet and kyanite index minerals are characteristic of the second event. Based on the thermobarometric data of sillimanite-bearing samples, a 650–680 °C and 500–600 MPa metamorphic peak is calculated, during which sillimanite formed. Considering these results, a polymetamorphic, clockwise *P–T* path can be constructed for the gneiss and mica schist that avoids the andalusite stability field.

By contrast, Lelkes-Felvári et al. (2003, 2005) assumed an initial high temperature/low pressure (HT/LP) amphibolite facies metamorphic event. In their model, garnet and andalusite formed under HT/LP conditions, whereas the second event within the amphibolite facies was responsible for the transformation of andalusite porphyroblasts into kyanite aggregates. According to this assumption, the garnet-kyanite-bearing gneisses could be characterized by a counterclockwise *P–T* path.

Lelkes-Felvári et al. (2003) defined the first metamorphic event in the AH to be of Permo-Triassic age (273 ± 7 Ma), established by garnet Sm–Nd data. Based on secondary muscovite Ar–Ar plateau ages, a Late Cretaceous (82–95 Ma) event is recognized as well and is interpreted as an Eo-Alpine regional metamorphic overprint. Balogh and Pécskay (2001) also published white mica Ar–Ar plateau Cretaceous ages (68.4–84.3 Ma) from the AH area. Horváth and Árkai (2002) agreed with the presence of the second Alpine metamorphic event.

Tari et al. (1999) documented a Cretaceous compressional phase in this region that resulted in nappe movements both in the Mesozoic cover and in the crystalline basement. These movements could have been responsible for the juxtaposition of blocks with different metamorphic histories in the adjacent Dorozsma High (DH). From top to bottom, garnetiferous kyanite gneiss-, dolomite marble- and amphibolite-dominated blocks have been described (M Tóth, 2008; M Tóth and Vargáne Tóth, 2020). During the Late Cretaceous, the entire region was subject to intrusions by granite and granodiorite ('banatite') bodies (Szalay, 1977; Szederkényi, 1984; Berza et al., 1998). Szederkényi (1984) described crystalline schists and gneisses from this area with a significant contact metasomatic, pneumatolytic overprint characterized by the presence of late muscovite and tourmaline as well as positive bulk Mo, Sn and W anomalies. The formations of secondary muscovite, post-kinematic tourmaline and polymetallic sulfide ore mineralization in the rocks of the neighboring DH are also interpreted as products of contact metasomatism related to these intrusions (M. Tóth, 2008). These intrusions are considered to be members of the Late Cretaceous arcuate banatite belt that extends from the Apuseni Mountains to the Black Sea (Neubauer, 2002).

Numerous geophysical interpretations (Rumpler and Horváth, 1988; Posgay et al., 1996; Tari et al. 1999) show that the AH has a metamorphic core complex structure formed by Miocene syn-rift extensional processes and the DH represents one of the tilted blocks in its background. Presence of a Miocene core complex is also suggested by Middle Miocene 17 ± 0.8 Ma zircon fission-track ages for gneiss samples of the AH that increase towards the adjacent DH (232 Ma) (Tari et al., 1999).

During the Pannonian Basin subsidence, the AH area was buried by thick Neogene sedimentary sequences, which are the most essential sources of hydrocarbons in the southeastern part of Hungary. Based on a previously applied model, the hydrocarbons likely migrated from the overpressured deep sub-basins toward the top zones of the

higher structural regimes (M. Tóth et al., 2007; Vass et al., 2018). Along the migration pathway, these fluids may have accumulated in the fracture system of the crystalline basement as well (M Tóth, 2008; M Tóth and Vargáne Tóth, 2020; Molnár et al., 2015; Nagy et al., 2013; Schubert et al., 2007). Although the metamorphic basement of the AH is an essential part of the petroleum system of the area, its role in fluid storage and migration is essentially unknown.

METHODS

The AH can only be investigated using cores and well-logging geophysics. In the last decades, close to 100 hydrocarbon exploratory boreholes reached the crystalline basement at about 2,500–3,000 m below the present surface; however, only 75 of them could provide samples for petrographic study. Furthermore, bulk rock major element compositions of 87 samples are available from previous work (Szederkényi, 1991).

Petrographic analysis

For a comprehensive petrographic study, close to 500 thin sections representing all 75 boreholes were investigated. If a grain was not identifiable by its optical properties, Raman spectroscopy analysis was conducted at the Department of Mineralogy, Geochemistry and Petrology at the University of Szeged using a THERMO DXR Raman microscope. For the measurement, 50x objective was used, and data were collected for 90 s with 5 mW power output and 2.1 μm laser spot size with a green laser source (532 nm, Nd-YAG). The main purpose of the micro-scale investigations was to obtain the mineral assemblages and the microtextural and microstructural characteristics of the samples. Based on the results, the overall rock identification and classification could be accomplished. Thanks to the recognition of mineral paragenesis and microtextural features, qualitative metamorphic history could be determined for each rock type, contributing to an appropriate reconstruction of the metamorphic evolution of the AH area.

Major element geochemistry

The main purpose of the evaluation of whole-rock major element data is to provide a reliable protolith estimation of the lithologies. To do so, three types of discriminant diagrams were applied to reveal the protolith character of the studied metamorphic rocks. By combining the petrographic properties of the main lithologies and the results of the discriminant diagrams, their igneous or sedimentary origin can be specified.

Estimation of P–T conditions

The *P–T* conditions of mineral paragenesis were estimated with the TWQ 2.3 software (Berman, 1991). This computer program permits calculating the positions of the possible

metamorphic reactions in *P–T* space. For calculation, those chemical systems were used that describe the paragenesis of the studied microtextural domains. Since the chemical compositions of most phases are not known, end-member reactions were computed.

Mapping

As a first step, the typical rock type of each borehole was marked on a point map, projected to the surface of the basement. From the point map, a lithologic map could be created by outlining the spatial extension of data points with some uncertainties. The expected spatial extension of the main litho-types was marked with distinct colors on the lithologic map. Finally, blocks of distinct rock types that experienced different metamorphic evolution were divided by theoretical structural boundaries (fault zones).

PETROGRAPHY

The most important petrographic features of the rock types are summarized in Table 1.

Garnet-kyanite gneiss, mica schist

Porphyroblastic gneiss and lepidoblastic mica schist contain quartz, potassium and plagioclase feldspars, biotite and muscovite with associated garnet porphyroblasts and fine-grained kyanite aggregates. Accessory minerals include rutile, ilmenite and zircon. In a few samples, idioblastic tourmaline and apatite, as well as epidote aggregates, are also visible (Fig. 2a).

Two types of texturally different biotite and muscovite flakes are recognizable. Smaller crystals define the main foliation (S2), whereas larger flakes (>200–400 μm) surround garnet grains and kyanite aggregates. Some of the large mica flakes contain inclusions of non-oriented kyanite crystals. Several large feldspar grains enclose quartz crystals and mica flakes. Garnet grains appear as large porphyroblasts with quartz, rutile and ilmenite inclusions wrapped by the main foliation (S2). Inclusion trails of elongated garnet grains, as well as biotite flakes in the pressure shadows of garnet, suggest a pre-kinematic foliation (S1) (Fig. 2b). Small, idioblastic garnet grains occur as well, resulting in a typical bimodal grain size distribution for garnet in gneiss and mica schist (Fig. 2c). Fine-grained kyanite aggregates usually appear adjacent to large garnet blasts or form pseudomorphs after garnet (Fig. 2d, e). Generally, the aggregates aligned parallel to the main foliation plane (S2) are defined by biotite flakes (Fig. 2e). Tourmaline and apatite crystals are undeformed and appear unoriented or align along the S2 foliation.

In the intensely deformed samples, quartz grains are strongly sutured, recrystallized and appear in bands elongated parallel to the S2 foliation. In some samples, kyanite inclusions are embedded in recrystallized quartz ribbons. Several feldspar grains are sub-grained. The mantles of asymmetric feldspar δ -clasts contain feldspar (Fig. 2f) and/



Table 1. Summary of petrographic features of the rock types

Rock type	Protolith	M1 (index mineral)	M2 (index mineral)	D1	D2	D3	Hydrothermal overprint
Garnet-kyanite gneiss	Sedimentary rocks	grt+bt+rt	ky+bt±grt	S1 foliation	S2 foliation and mylonitization	brittle deformation-fault breccia, cataclasis	Tourmaline, apatite, epidote
Garnetiferous amphibolite	Igneous rocks	amp+grt+bt+rt	-	S1 foliation	-	-	-
Epidote gneiss	Igneous rocks	ep+chl+ser	-	S1 foliation and mylonitization	-	-	-
Chlorite schist	Igneous rocks	chl±bt	-	S1 foliation	Shearing mylonitization	-	Ore minerals, propylitic alteration
Greenschist	Igneous rocks	chl+act+ep	-	S1 foliation	-	-	-

or quartz aggregates with polygonal microtextures (Fig. 2g). Boudinage-textured garnet grains are sheared toward the S2 foliation direction (Fig. 2h). Garnet δ -clasts (Fig. 3a), muscovite and biotite mica fishes, as well as S-C fabrics (Fig. 3b), are relatively abundant in most samples. The chloritization of garnet and biotite, the reaction of kyanite to white mica and sericitization and saussuritization of feldspar grains are the most typical retrograde alterations.

Garnetiferous amphibolite

Garnet-rich amphibolites are slightly oriented and exhibit nematoblastic/poikiloblastic textures. Samples commonly consist of green or dark brown prismatic amphibole crystals that are occasionally xenoblastic and large, inclusion-rich resorbed garnet blasts (Fig. 3c). Less frequent phases are quartz, plagioclase feldspar and biotite. Quartz, amphibole and rutile are inclusions in garnet (Fig. 3d). Amphibole grains are optically zoned with dark brown cores and light green or white rims (Fig. 3e) and frequently exhibit signs of moderate chloritization and carbonatization. Accessory minerals include rutile, titanite and hematite, with rutile needles fringed by titanite (Fig. 3f).

Epidote gneiss

The rock-forming minerals of these gneissose rocks are quartz, plagioclase and potassium feldspars, muscovite and chloritized biotite. In some specimens, epidote and clinozoisite also occur as rock-forming constituents. Accessory minerals are rutile, zircon, apatite, titanite and magnetite.

Biotite, muscovite and quartz bands define the rock foliation. Both the dominant plagioclase and subordinate, sericitized K-feldspar form large, idiomorphic crystals. Some feldspar grains are myrmekitic (Fig. 3g) and form polygonal textures (Fig. 3h). Coarse-grained quartz lenses with polygonal texture are also frequent. Zircon is found as idiomorphic crystals (Fig. 4a). In the intensively deformed samples, quartz grains are strongly sutured and the feldspar is mostly present as asymmetric δ -clasts (Fig. 4b) or mantled by polygonal quartz aggregates (Fig. 4c). In some samples, quartz and muscovite reaction rims developed around feldspar grains.

Two types of texturally different epidote and clinozoisite can be distinguished, including small, idiomorphic crystals that occur parallel to the foliation (Fig. 4d) and aggregates of large grains that are probably pseudomorphs after feldspar (Fig. 4e). These types of grains are wrapped by the foliation.

Chlorite schist

The well-foliated schistose rocks have a lepidoblastic texture, where chlorite and quartz are the primary rock-forming minerals. The mineral assemblage also includes biotite, K-feldspar, calcite, epidote, siderite aggregates and accessory rutile, apatite and titanite rimmed by rutile.

Foliation in these rocks is defined by chlorite rods. Sporadic instances of biotite having formed on the rims of chlorite flakes have been observed (Fig. 4f). Quartz grains

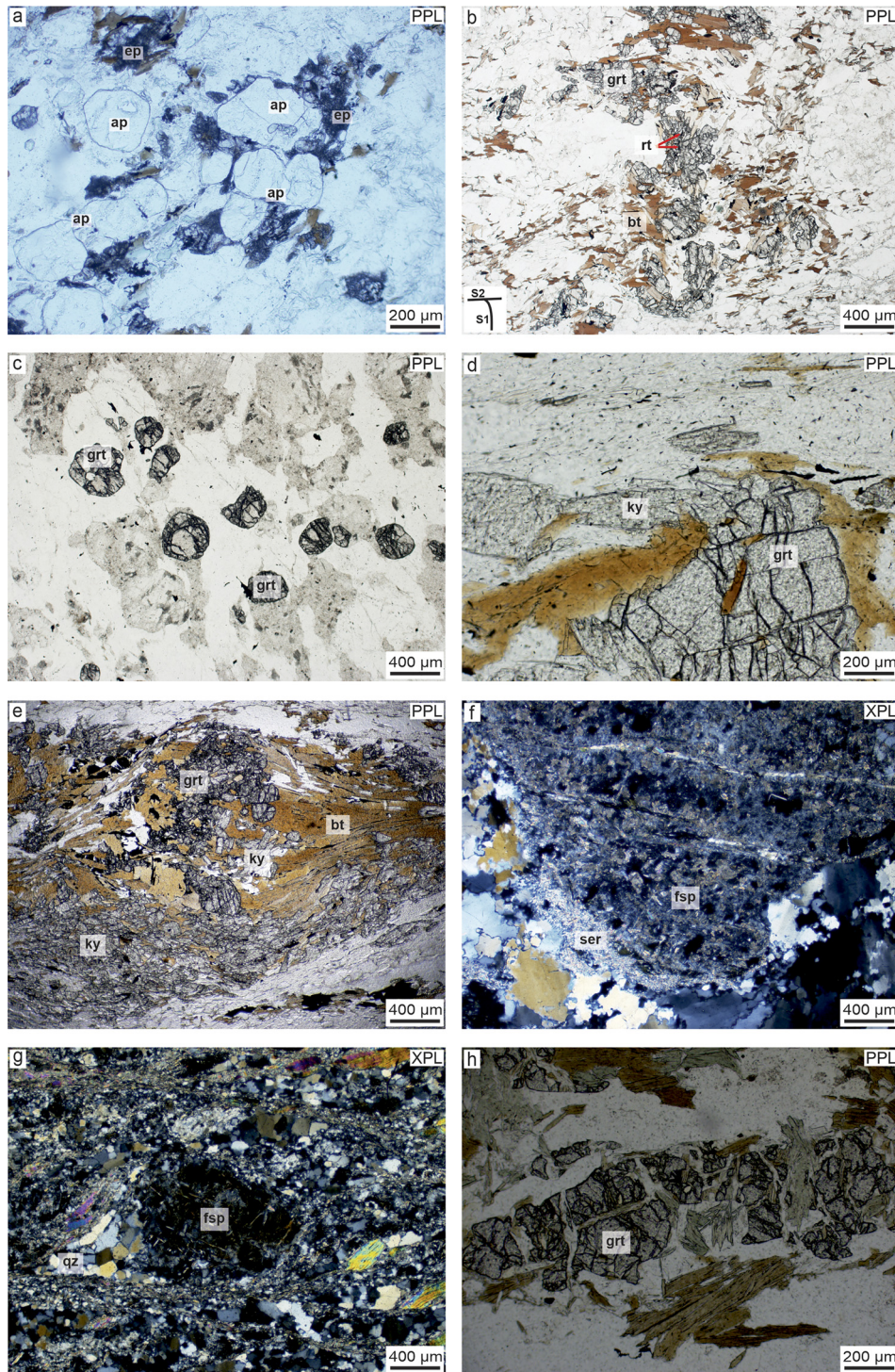


Fig. 2. Petrographic features of the garnet-kyanite gneiss and mica schist. (a) apatite crystals and epidote aggregates; (b) inclusion trails of elongated garnet grain; (c) small, idioblastic garnet grains; (d) pseudomorphic kyanite aggregate after garnet; (e) kyanite aggregates align parallel to the S2 foliation plane; (f) feldspar σ -clast; (g) feldspar σ -clast associated quartz aggregates with polygonal microtexture; (h) boudinage textured garnet grain. Mineral abbreviations after [Whitney and Evans \(2010\)](#)

inside the chlorite matrix are small and have a rounded shape. Calcite often forms polygonal aggregates in lenses ([Fig. 4g](#)) or is adjusted parallel to the foliation planes.

Prismatic, idioblastic epidote crystals and siderite aggregates run along the chlorite rods in the direction of the

foliation planes ([Fig. 4h](#)). Opaque minerals are quite abundant and appear disseminated or oriented along the weakness planes and are identified as magnetite, pyrite and chalcopyrite based on Raman spectroscopic analysis ([Fig. 6](#)). Disseminated grains are idiomorphic, undeformed and

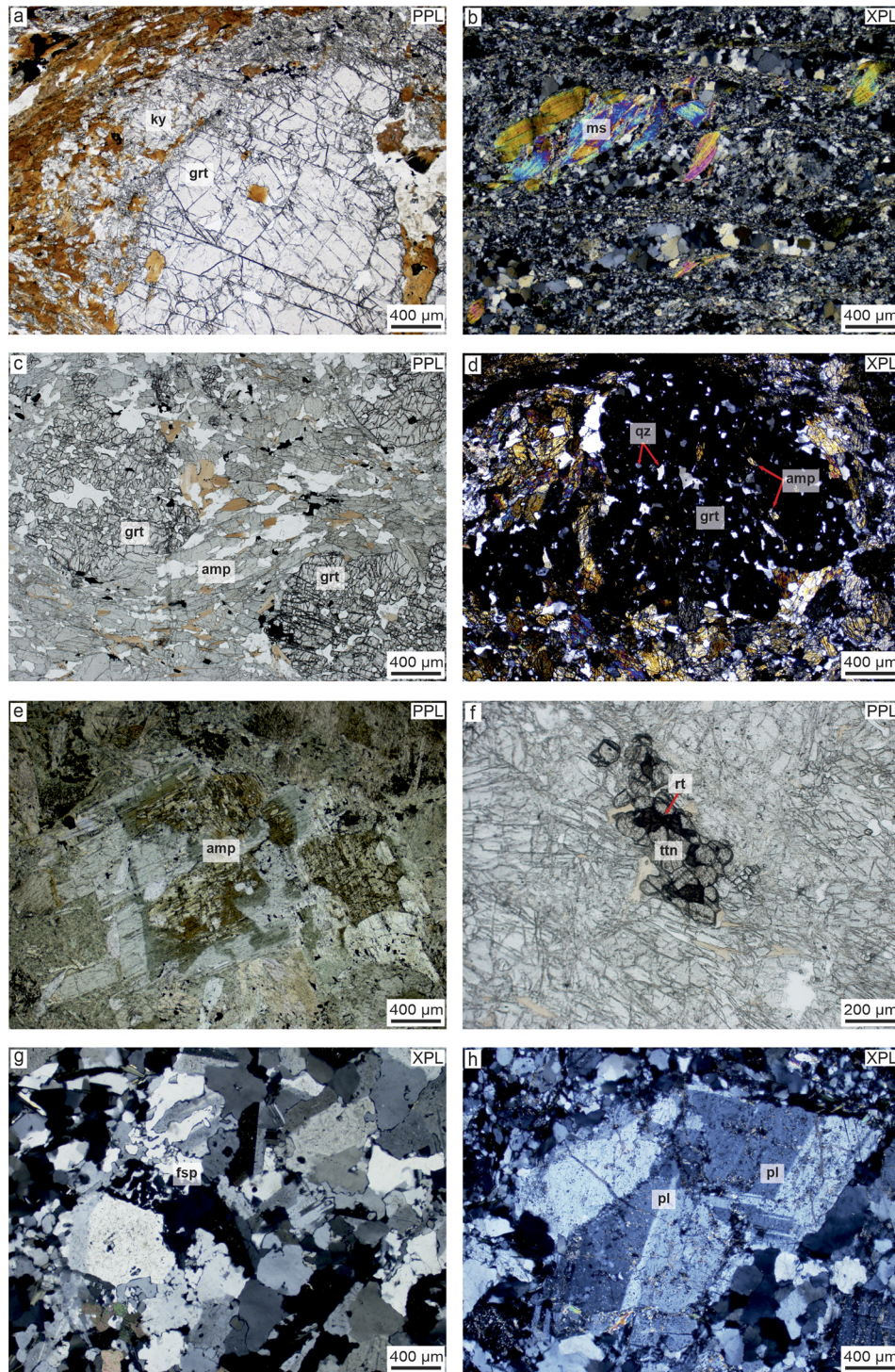


Fig. 3. Petrographic features of garnet-kyanite gneiss, mica schist, garnetiferous amphibolite and epidote gneiss. (a) garnet σ -clast mantled by kyanite aggregates; (b) mica fishes and S–C fabrics; (c) oriented amphibole crystals and inclusion-rich resorbed garnet blast; (d) inclusions in garnet; (e) optically zoned amphibole grains; (f) rutile needles fringed by titanite; (g) myrmekitic feldspar; (h) feldspar forms polygonal texture. Mineral abbreviations after [Whitney and Evans \(2010\)](#)

unwrapped by the foliation plane. Some ore mineral grains have a sheared and boudinage microtexture. In some samples, non-oriented, fibrous calcite strain fringes grew around rigid opaque minerals ([Fig. 5a](#)). Microfolding of pre-existing foliation planes (S1) resulted in crenulation cleavage ([Fig. 5b](#)).

Greenschist

Greenschists are slightly foliated, nematoblastic, fine-grained rocks that consist of chlorite, idioblastic/hypidioblastic epidote, clinozoisite and small light green actinolite crystals

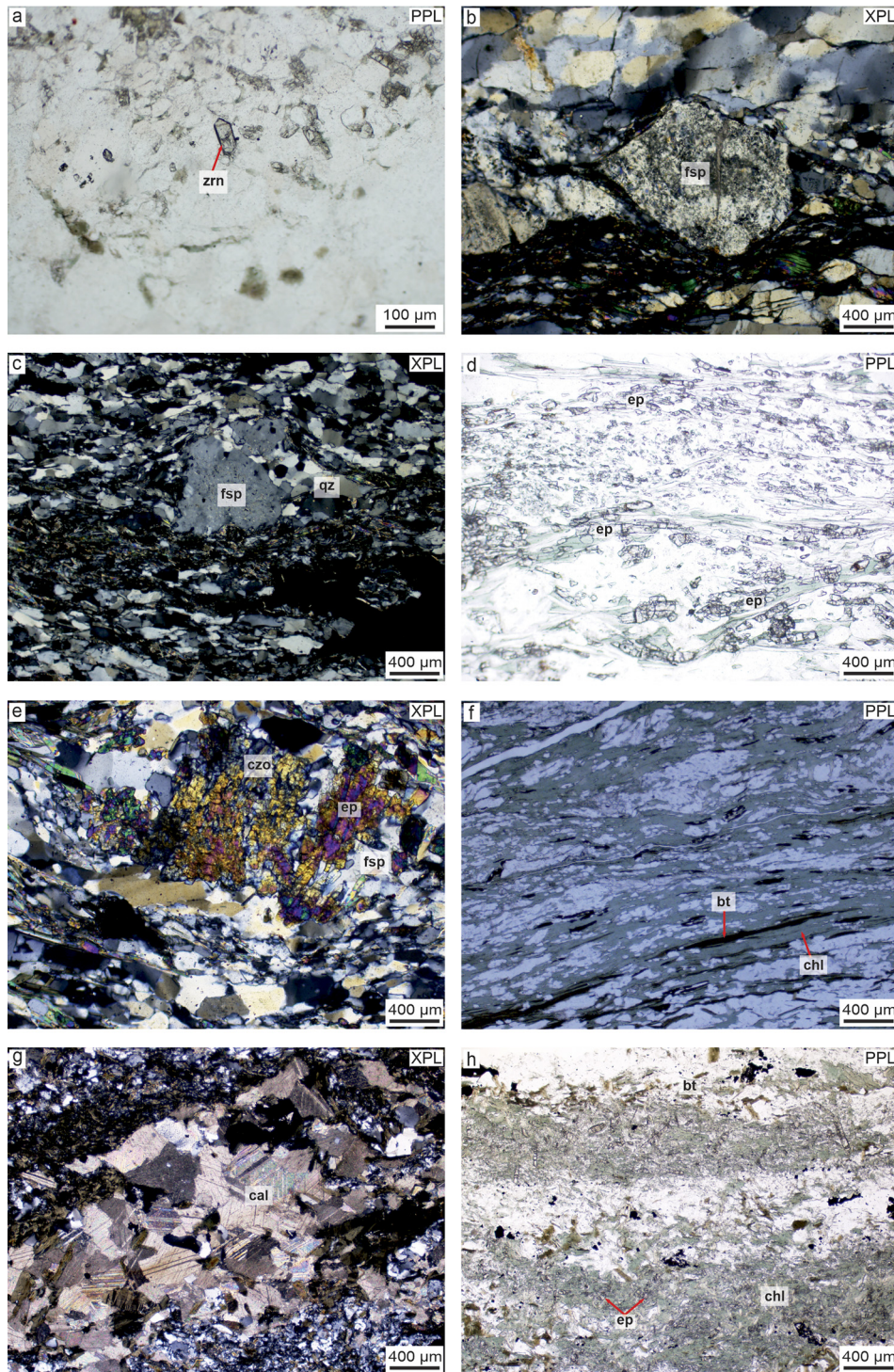


Fig. 4. Petrographic features of epidote gneiss and chlorite schist. (a) idiomorphic zircon crystal; (b) feldspar σ -clast; (c) feldspar σ -clast mantled by polygonal quartz aggregates; (d) idiomorphic epidote crystals parallel to the foliation; (e) epidote pseudomorphs after feldspar; (f) foliation plane defined by chlorite rods with biotite flakes; (g) lens of polygonal calcite; (h) epidote crystals run along the chlorite rods. Mineral abbreviations after [Whitney and Evans \(2010\)](#)

exhibiting radiating blades associated with quartz, feldspar and calcite ([Fig. 5c, d](#)). Accessory phases are titanite and magnetite. In some larger amphibole crystals, epidote inclusions can be found ([Fig. 5e](#)).

Fault breccia and cataclasite

Clast-dominated fault breccias comprised a chaotic distribution of angular fragments set in a carbonate-rich matrix.

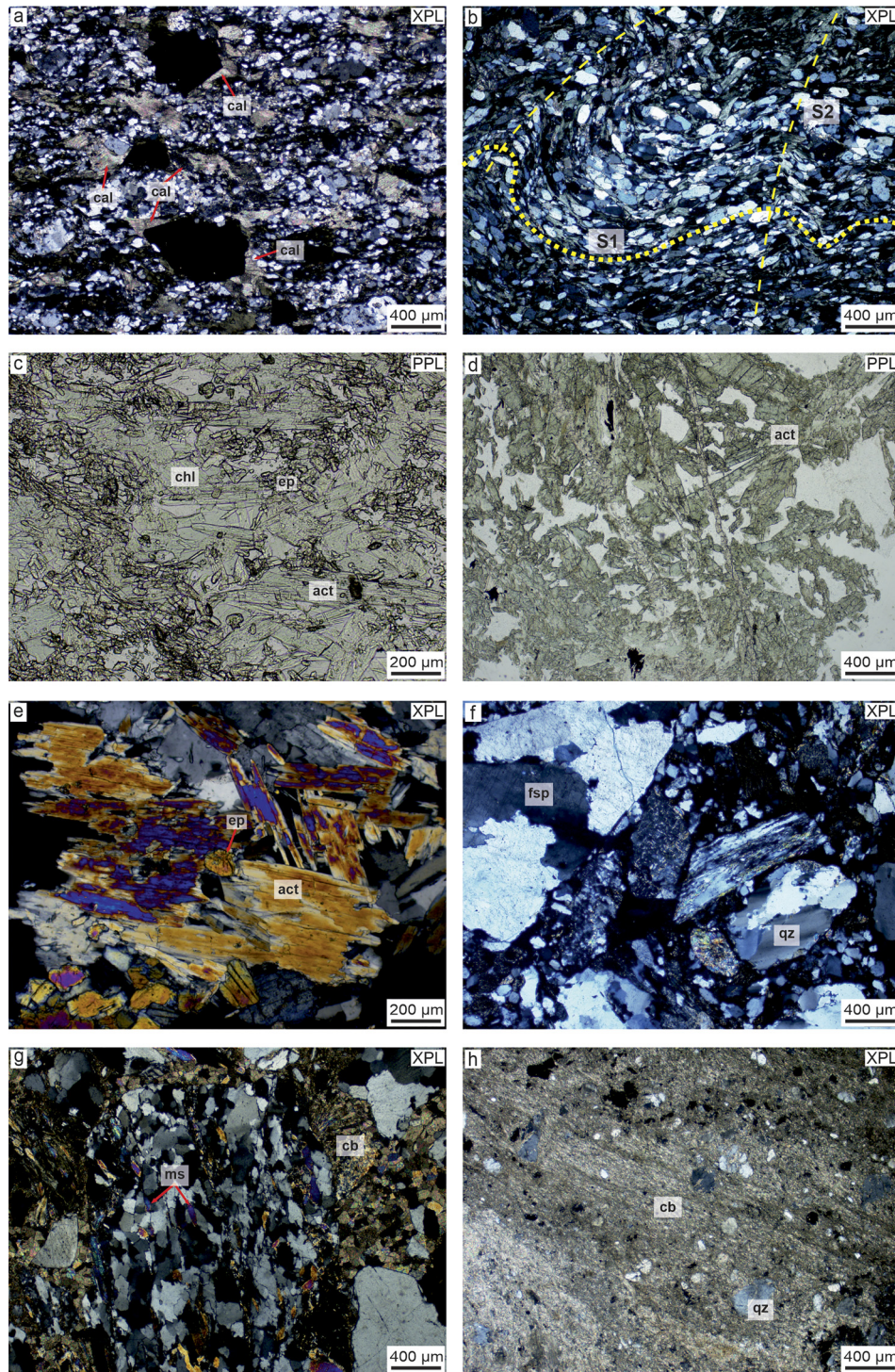


Fig. 5. Petrographic features of chlorite schist, greenschist and tectonites. (a) strain fringes structure; (b) crenulation cleavage; (c) fine-grained actinolite and epidote; (d) radiating blades of actinolite crystals; (e) epidote inclusions in amphibole crystals; (f) quartz grains of rock fragments; (g) mica fishes in clasts; (h) quartz clasts with carbonate cement of cataclasite. Mineral abbreviations after [Whitney and Evans \(2010\)](#)

Gneiss, as a precursor lithology, is recognizable in the fragments characterized by quartz, feldspar, muscovite and biotite. Quartz grains of the rock fragments are aligned parallel to the oriented muscovite and biotite bands ([Fig. 5f](#)). In some clasts, mica fish also occurs

([Fig. 5g](#)). Cataclasites have a smaller clast diameter and a higher matrix proportion compared with the fault breccias. The clast material is monomineralic and consists mainly of quartz or feldspar, with carbonate cement ([Fig. 5h](#)).

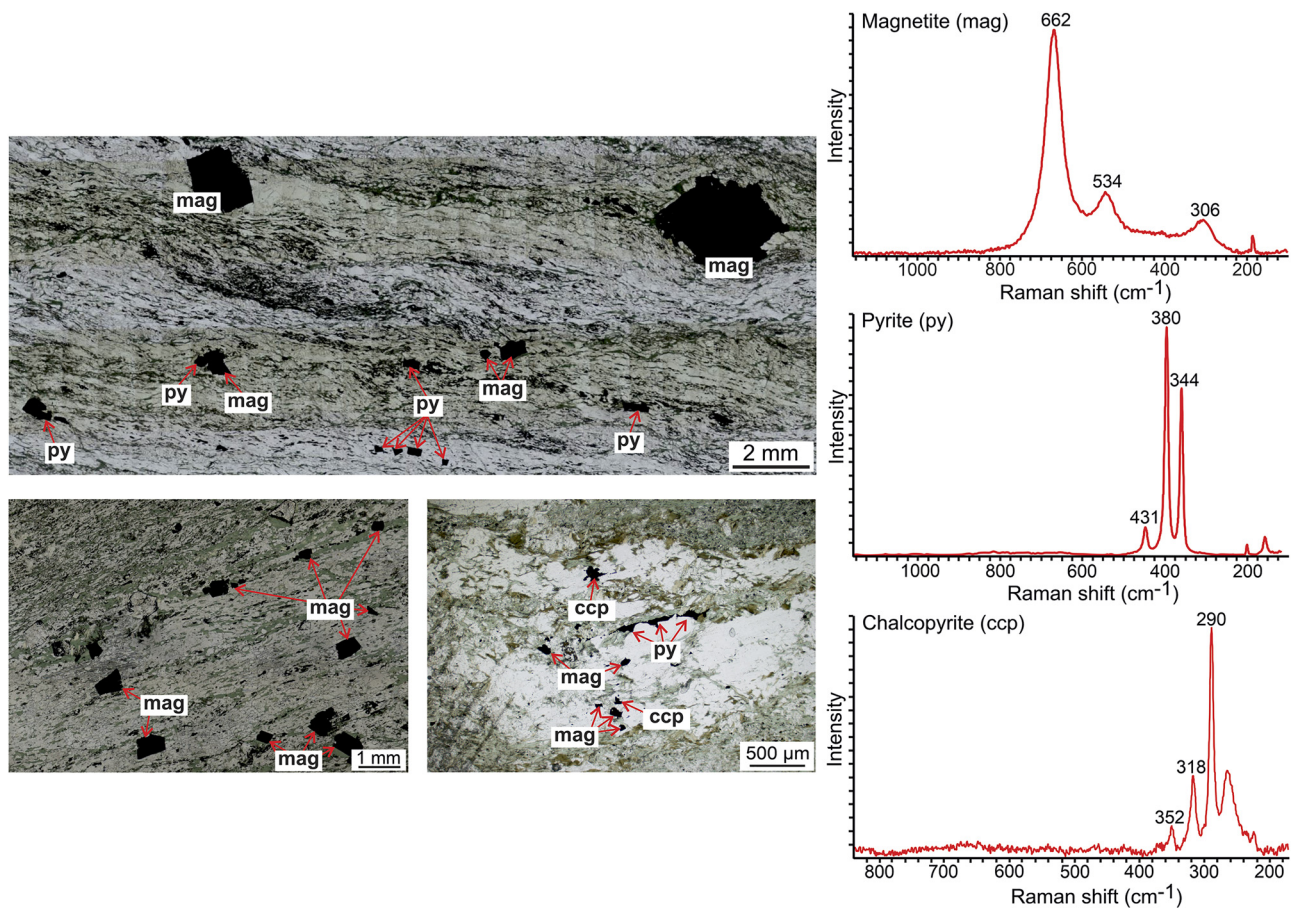


Fig. 6. Typical Raman spectra of measured opaque crystals of the chlorite schist. The characteristics Raman peaks of magnetite, pyrite and chalcopyrite at the given wavenumbers (cm^{-1}) are marked on the spectra. Mineral abbreviations after Whitney and Evans (2010)

GEOCHEMISTRY

The major element compositions of samples included in the present study were collected by Szederkényi (1991) and are listed in Table 2. For the gneisses and chlorite schists, the SiO_2 vs. TiO_2 (Shan et al., 2016) and the $\text{K}_2\text{O}/\text{Al}_2\text{O}_3$ vs. $\text{Na}_2\text{O}/\text{Al}_2\text{O}_3$ (Garrels and Mackenzie, 1971) discrimination diagrams were used to identify the protolith of the para-metamorphic and orthometamorphic rocks. All garnet-kyanite gneisses plot within the sedimentary field, whereas samples of epidote gneiss and chlorite schist mainly fall in the igneous field (Fig. 7). Based on the CaO-MgO-FeO^T ternary diagram (Misra, 1971), the garnetiferous amphibolite and greenschist samples are classified as orthoamphibolites (Fig. 8).

DISCUSSION

Petrological interpretation

According to petrographic study, the AH consists of five dominant petrographic groups: garnet-kyanite gneiss and mica schist, garnetiferous amphibolite, epidote gneiss, chlorite schist and greenschist. Some boreholes also

sampled tectonites of these rock types as fault breccia and cataclasite.

Garnet-kyanite gneiss and mica schist are the most common lithologies. Relic biotite flakes along with large, inclusion-rich, sheared garnet porphyroblasts and rutile grains denote the first metamorphic stage (M1). According to Horváth and Árkai (2002), the first metamorphic stage can be characterized by 820–1,010 MPa and 520–560 °C P - T conditions in the presence of staurolite and occurred during the Permian (273 ± 7 Ma, Lelkes-Felvári et al., 2003). The elongated garnet grains associated with inclusion trails and biotite flakes located in the pressure shadow zone of garnet suggest development of an early foliation plane (S1) caused by the first deformation phase (D1). Small, inclusion-free, idioblastic garnet grains are interpreted as the second generation of garnet. Fine-grained kyanite aggregates appear next to rims of the initial garnets or lie parallel to the main foliation plane (S2) as defined by muscovite and biotite flakes. The observed fine-grained phases (biotite, garnet and kyanite) represent the second stage of metamorphism (M2).

Although suggested by observed textures, the interpretation of the direct replacement of garnet porphyroblasts by fine-grained kyanite aggregates is problematic. One possible interpretation of this microtexture is that fibrolite (sillimanite) first replaced garnet porphyroblasts, which later

Table 2. Whole-rock major element data (in wt%) of the studied samples collected by Szederkényi (1991)

Borehole	Core	Depth (m)	SiO ₂	TiO ₂	Al ₂ O ₃	Fe ₂ O ₃	FeO	MnO	MgO	CaO	Na ₂ O	K ₂ O	H ₂ O	P ₂ O ₅	CO ₂	S	Σ	FeO ^T	Na ₂ O/Al ₂ O ₃	K ₂ O/Al ₂ O ₃	
Garnet-kyanite gneiss, micaschist																					
A-19.	11.	3,077–3,083	73.15	0.57	13.07	0.57	1.69	0.03	0.80	1.96	3.93	1.44	1.51	0.06	0.72	0.00	99.50	2.43	0.30	0.11	
A-27.	6.	3,144–3,146	68.77	0.26	12.89	1.83	4.08	0.09	1.03	3.04	3.96	0.84	0.59	0.09	2.46	0.00	99.93	6.32	0.31	0.07	
A-15.	18.	2,916–2,917	48.79	0.52	15.92	2.34	5.66	0.19	4.61	7.41	2.73	1.95	4.00	0.15	5.27	0.08	99.62	8.57	0.17	0.12	
A-82.	8.	2,697–2,698	50.20	0.82	15.85	3.48	7.09	0.11	4.45	5.90	2.16	0.85	5.22	0.08	4.61	0.00	100.82	11.28	0.14	0.05	
A-83.	5.	2,802–2,803	66.91	0.00	16.44	1.23	3.89	0.11	1.15	2.50	4.32	0.57	2.52	0.68	0.67	0.00	100.99	5.51	0.26	0.03	
A-4.	31.	2,679–2,681	64.26	0.71	17.46	1.24	3.88	0.08	1.47	0.98	2.06	4.15	3.01	0.12	0.07	0.14	99.63	5.51	0.12	0.24	
A-4.	32.	2,704–2,705	62.08	0.47	17.15	1.44	4.00	0.08	2.45	2.80	4.35	2.55	2.13	0.22	0.21	0.07	100.00	5.84	0.25	0.15	
A-84.	9/1.	2,672–2,673	66.20	0.57	18.11	0.02	4.07	0.00	1.02	1.28	2.43	2.82	3.24	0.08	0.90	0.00	100.74	4.50	0.13	0.16	
A-62.	17/2.	2,730–2,736	52.61	0.80	24.96	1.11	5.93	0.11	2.03	0.67	0.98	5.75	4.82	0.06	0.00	0.16	99.99	7.63	0.04	0.23	
A-62.	17/3.	2,730–2,736	57.92	1.81	20.90	0.82	5.69	0.09	2.19	0.70	0.83	3.78	3.91	0.03	0.05	0.19	98.91	7.08	0.04	0.18	
A-115.	7.	2,606–2,607	62.55	0.78	19.31	1.35	5.11	0.18	1.53	1.36	1.32	3.96	2.22	0.09	0.13	0.00	99.89	6.97	0.07	0.21	
A-116.	6.	2,564–2,566	64.64	0.49	15.89	0.63	4.53	0.16	1.40	2.71	3.24	2.22	2.65	0.08	1.15	0.00	99.79	5.61	0.20	0.14	
A-264.	10/1.	2,553–2,556	60.63	0.59	15.09	0.64	7.18	0.14	2.84	3.10	2.67	2.07	3.46	0.22	1.15	0.00	99.78	8.54	0.18	0.14	
A-264.	10/2.	2,553–2,556	56.77	0.34	17.92	0.72	6.83	0.09	3.21	2.33	2.40	3.18	4.05	0.15	1.17	0.00	99.16	8.23	0.13	0.18	
A-264.	11.	2,556–2,557	65.13	0.67	14.05	0.20	6.19	0.15	2.35	2.46	2.61	2.10	2.56	0.27	1.58	0.00	100.32	7.01	0.19	0.15	
A-28.	16/2.	2,773–2,778	54.87	0.68	23.37	2.62	6.63	0.17	1.41	0.89	1.21	3.00	4.52	0.09	0.23	0.00	99.69	9.91	0.05	0.13	
A-109.	9.	2,609–2,611	58.80	0.73	16.34	0.49	5.42	0.15	2.06	5.54	3.48	2.34	2.80	0.80	0.76	0.03	99.74	6.45	0.21	0.14	
A-40.	11.	2,662–2,666	62.52	0.50	12.85	0.89	5.01	0.04	2.17	1.06	2.66	3.12	3.49	0.04	0.46	0.00	94.81	6.40	0.21	0.24	
A-97.	5/2.	1,545–1,546	50.88	1.03	16.93	1.06	10.57	0.33	5.24	1.71	2.60	1.38	6.68	0.71	1.13	0.00	100.25	12.69	0.15	0.08	
A-64.	4.	3,027–3,028	70.88	0.09	12.97	1.34	3.79	0.11	2.47	1.50	2.49	1.44	2.81	0.03	0.14	0.00	100.06	5.51	0.19	0.11	
A-85.	6.	2,926–2,928	48.80	1.40	15.50	2.23	6.01	0.16	5.61	5.04	3.20	2.00	5.40	0.21	3.79	0.57	99.92	8.84	0.21	0.13	
A-85.	8.	3,028–3,030	65.93	0.24	17.42	0.47	2.08	0.11	1.67	1.14	0.61	4.29	2.58	0.11	2.54	0.00	99.19	2.76	0.04	0.25	
A-17.	8/2.	2,881–2,886	61.53	0.66	18.54	1.51	4.72	0.08	2.06	0.84	1.87	3.33	4.08	0.15	0.19	0.67	100.23	6.70	0.10	0.18	
A-17.	9.	2,886–2,893	69.68	0.55	14.80	0.95	3.39	0.00	1.40	1.12	2.14	2.43	2.99	0.27	0.11	0.46	100.29	4.68	0.14	0.16	
A-90.	6/2.	2,620–2,623	57.42	0.91	20.84	0.77	6.80	0.05	2.05	1.44	1.15	4.92	4.00	0.08	0.09	0.00	100.52	8.25	0.06	0.24	
A-91.	4/5.	2,530–2,539	58.20	0.80	22.71	0.56	6.25	0.04	1.28	0.89	1.00	3.84	4.44	0.11	0.68	0.00	100.80	7.44	0.04	0.17	
A-91.	5.	2,560–2,563	54.13	0.77	23.94	1.56	5.66	0.04	0.96	0.88	0.93	4.47	5.76	0.69	0.57	0.00	100.36	7.79	0.04	0.19	
A-92.	4.	2,562–2,563	72.37	0.10	15.72	0.34	2.07	0.00	0.32	0.80	1.41	4.83	2.02	0.04	0.14	0.00	100.16	2.62	0.09	0.31	
A-95.	3.	2,490–2,493	63.96	0.87	15.19	0.47	5.53	0.11	2.45	1.93	2.37	4.50	2.69	0.21	0.28	0.00	100.56	6.55	0.16	0.30	
A-95.	4.	2,512–2,514	60.29	0.84	18.73	0.62	6.31	0.17	1.78	1.80	2.37	4.50	2.77	0.11	0.16	0.00	100.45	7.56	0.13	0.24	
A-50.	11.	2,529–2,533	47.20	1.91	19.48	2.21	8.96	0.23	3.11	2.15	0.38	5.76	5.14	0.38	2.48	0.00	99.39	12.07	0.02	0.30	
A-51.	5.	2,496–2,500	50.15	0.90	26.15	0.41	8.04	0.32	2.31	0.72	1.59	3.78	3.12	0.06	0.98	0.00	98.53	9.25	0.06	0.14	
A-51.	6/1.	2,496–2,500	36.60	1.66	35.16	2.37	10.88	0.43	3.46	0.71	0.37	4.20	3.93	0.06	0.05	0.00	99.88	14.34	0.01	0.12	
A-51.	6/2.	2,529–2,530	47.85	2.09	16.55	3.19	7.31	0.16	5.61	8.30	3.48	1.44	1.65	1.27	0.53	0.00	99.43	11.23	0.21	0.09	
A-51.	7.	2,570–2,574	47.47	2.20	15.80	3.28	7.93	0.22	5.25	10.95	3.69	1.68	0.00	0.50	0.92	0.00	99.89	12.00	0.23	0.11	
A-31.	6.	2,505–2,510	71.69	0.00	17.85	0.37	0.84	0.00	0.40	0.56	0.65	5.25	2.47	0.09	0.04	0.00	100.21	1.29	0.04	0.29	
A-31.	8.	2,510–2,511	58.14	0.77	21.10	1.69	4.60	0.00	1.37	0.37	1.30	5.43	4.30	0.09	0.25	0.00	99.41	6.75	0.06	0.26	
A-78.	4.	2,546–2,548	54.62	0.89	21.91	2.01	7.20	0.19	2.18	2.14	0.87	2.94	5.03	0.05	0.18	0.00	100.21	9.93	0.04	0.13	
A-94.	4.	2,605–2,606	44.76	1.12	28.21	0.94	9.39	0.18	2.66	0.58	0.83	5.87	4.81	0.05	0.82	0.00	100.22	11.27	0.03	0.21	
A-107.	2/2.	2,881–2,884	66.37	0.60	18.00	0.65	4.68	0.09	0.86	0.91	1.29	3.48	2.33	0.14	0.27	0.00	99.67	5.80	0.07	0.19	
A-53.	6.	2,635–2,641	57.85	0.74	21.24	1.87	7.52	0.18	0.77	0.91	0.93	3.33	3.57	0.12	1.27	0.00	100.30	10.14	0.04	0.16	

(continued)



**Table 2. Continued**

Borehole	Core	Depth (m)	SiO ₂	TiO ₂	Al ₂ O ₃	Fe ₂ O ₃	FeO	MnO	MgO	CaO	Na ₂ O	K ₂ O	H ₂ O	P ₂ O ₅	CO ₂	S	Σ	FeO ^T	Na ₂ O/Al ₂ O ₃	K ₂ O/Al ₂ O ₃	
A-52.	5.	2,524–2,528	61.65	1.66	19.25	1.07	5.04	0.11	1.95	1.12	1.17	2.73	2.53	0.08	0.07	0.14	98.57	6.61	0.06	0.14	
A-52.	6.	2,569–2,572	60.40	0.57	18.15	1.97	7.23	0.38	1.92	1.71	2.21	2.16	3.19	0.12	0.04	0.64	100.69	9.92	0.12	0.12	
A-55.	5.	2,520–2,524	72.56	0.00	16.52	0.84	0.60	0.04	0.22	1.11	3.81	2.22	1.57	0.25	0.00	0.00	99.74	1.50	0.23	0.13	
A-108.	5.	2,544–2,547	53.19	1.01	23.69	1.32	6.51	0.16	1.93	0.97	2.01	4.98	4.41	0.14	0.07	0.00	100.39	8.48	0.08	0.21	
A-59.	6/2.	2,581–2,582	54.25	0.93	21.88	1.66	6.42	0.38	1.78	1.37	2.42	4.20	4.81	0.24	0.42	0.00	100.76	8.72	0.11	0.19	
A-81.	8.	2,625–2,627	60.95	0.23	18.91	1.41	4.36	0.08	3.08	1.07	0.27	2.64	4.15	0.18	2.60	0.00	99.93	6.21	0.01	0.14	
Epidote gneiss																					
A-11.	5/1.	2,447–2,449	60.08	0.09	16.37	2.01	5.44	0.11	3.79	2.38	2.43	0.24	5.08	0.12	1.41	0.22	99.77	7.99	0.15	0.01	
A-11.	6.	2,575–2,576	65.81	0.09	17.30	2.58	1.14	0.11	1.33	3.13	3.21	2.25	2.26	0.04	0.32	0.91	100.48	3.83	0.19	0.13	
A-104.	7/2.	2,590–2,592	66.40	0.07	15.78	1.13	2.30	0.09	1.46	3.07	4.08	1.14	1.98	0.04	2.04	0.00	99.58	3.66	0.26	0.07	
A-249.	10/2.	2,510–2,512	73.49	0.06	12.29	0.14	3.40	0.09	2.83	1.08	4.41	0.31	2.28	0.10	0.11	0.00	100.59	3.88	0.36	0.03	
A-99.	10.	2,558–2,566	54.60	1.29	15.20	2.35	6.98	0.15	6.95	1.79	4.05	0.11	5.18	0.14	1.16	0.00	99.95	10.03	0.27	0.01	
A-99.	11.	2,577–2,578	71.10	0.30	12.20	1.93	1.54	0.04	1.25	2.45	3.52	1.41	2.01	0.06	1.66	1.10	100.57	3.62	0.29	0.12	
A-16.	21/1.	2,526–2,528	68.11	0.00	14.28	1.43	1.93	0.00	4.25	1.42	3.45	0.72	2.94	0.05	0.65	0.72	99.95	3.55	0.24	0.05	
A-16.	22.	2,560–2,561	69.01	0.00	14.19	0.21	1.79	0.00	4.37	1.96	4.21	0.58	3.38	0.08	0.11	0.04	99.93	2.18	0.30	0.04	
A-14.	21.	2,957–2,957	51.18	0.00	19.20	2.02	7.64	0.15	7.64	1.26	3.63	0.72	5.16	0.03	0.65	0.28	99.56	10.42	0.19	0.04	
A-103.	2.	2,444–2,447	73.99	0.00	12.22	0.96	2.50	0.10	1.28	3.73	3.18	0.71	1.52	0.05	0.22	0.00	100.46	3.71	0.26	0.06	
A-103.	3/2.	2,502–2,505	72.22	0.24	11.84	1.03	2.93	0.11	1.54	3.56	3.24	0.89	1.99	0.05	0.14	0.00	99.78	4.25	0.27	0.08	
A-68.	10/1.	2,662–2,665	67.85	0.00	16.39	1.17	1.90	0.11	1.28	3.22	2.95	1.99	2.00	0.03	1.33	0.00	100.22	3.26	0.18	0.12	
A-68.	10/2.	2,662–2,665	92.10	0.04	3.95	0.24	0.37	0.02	0.38	1.07	1.14	0.17	0.57	0.06	0.51	0.00	100.62	0.65	0.29	0.04	
Chlorite schist																					
A-87.	9.	2,620–2,625	49.35	0.74	15.97	3.15	7.88	0.05	5.52	4.46	2.32	4.41	6.09	0.06	3.95	0.00	103.95	11.82	0.15	0.28	
A-22.	13.	2,516–2,523	58.85	0.00	15.37	0.89	6.48	0.18	6.34	2.56	3.78	0.14	4.33	0.08	1.75	0.21	100.96	8.02	0.25	0.01	
A-22.	14.	2,523–2,535	62.66	0.00	12.36	1.51	4.26	0.08	3.06	5.59	2.58	0.30	3.34	0.04	3.90	0.02	99.70	6.20	0.21	0.02	
A-100.	10.	2,636–2,640	57.96	0.15	12.73	1.90	8.82	0.22	4.99	3.38	3.03	0.20	3.94	0.03	2.20	0.00	99.55	11.60	0.24	0.02	
A-100.	11.	2,648–2,649	40.63	0.82	14.93	2.04	8.61	0.17	7.16	8.72	2.55	0.56	3.86	0.45	10.02	0.00	100.52	11.51	0.17	0.04	
A-89.	12/1.	2,561–2,563	74.24	0.03	12.06	1.21	2.27	0.07	2.33	0.54	5.64	0.18	1.87	0.05	0.05	0.00	100.54	3.71	0.47	0.01	
A-89.	12/2.	2,561–2,563	54.76	0.18	15.21	3.82	10.00	0.17	6.17	0.53	2.19	0.32	6.84	0.06	0.11	0.00	100.36	14.82	0.14	0.02	
A-70.	4/2.	2,469–2,470	64.35	0.23	13.53	0.72	6.26	0.11	1.14	2.68	4.08	0.76	1.56	0.07	4.63	0.00	100.12	7.61	0.30	0.06	
A-70.	5.	2,547–2,548	69.08	0.27	14.56	2.55	2.06	0.11	1.15	5.36	2.43	0.76	1.90	0.06	0.28	0.00	100.57	4.82	0.17	0.05	
A-88.	9.	2,707–2,709	69.71	0.34	14.01	1.92	2.56	0.00	0.89	1.23	5.97	1.29	2.16	0.13	0.10	0.00	100.31	4.74	0.43	0.09	
A-72.	6.	2,765–2,767	69.05	0.00	15.32	1.30	3.23	0.11	1.67	2.11	2.19	1.88	3.07	0.05	0.14	0.00	100.12	4.85	0.14	0.12	
A-105.	7.	2,914–2,919	71.15	0.12	14.75	2.87	1.07	0.08	0.20	0.42	4.53	1.71	2.95	0.03	0.00	2.05	101.93	4.05	0.31	0.12	
A-71.	9.	2,538–2,549	57.40	0.64	14.60	3.01	7.64	0.19	6.66	0.42	3.49	0.20	5.12	0.05	0.09	0.00	99.51	11.41	0.24	0.01	
A-71.	11.	2,558–2,561	54.91	0.22	16.09	2.30	9.20	0.31	7.19	2.14	2.19	0.24	5.73	0.04	0.18	0.00	100.74	12.42	0.14	0.01	
Garnetiferous amphibolite																					
A-62.	18/1.	2,744–2,746	54.99	1.05	16.13	1.69	6.66	0.20	5.96	5.32	1.02	2.70	2.37	0.13	1.10	0.00	99.32	9.02	0.06	0.17	
A-62.	18/2.	2,744–2,746	60.19	0.80	19.86	1.78	5.22	0.11	2.35	0.84	0.22	4.62	3.52	0.18	0.06	1.16	100.91	7.52	0.01	0.23	
A-444.	3.	2,485–2,488	54.20	1.28	9.08	2.05	6.98	0.16	11.60	4.32	1.54	0.31	5.97	0.32	1.53	0.00	99.34	9.73	0.17	0.03	
Greenschist																					
A-69.	10/1.	2,684–2,687	44.30	0.13	17.93	4.48	3.48	0.21	8.52	8.35	1.17	0.21	5.80	0.01	1.59	0.00	99.18	8.31	0.07	0.01	

(continued)

Table 2. Continued

Borehole	Core	Depth (m)	SiO ₂	TiO ₂	Al ₂ O ₃	Fe ₂ O ₃	FeO	MnO	MgO	CaO	Na ₂ O	K ₂ O	H ₂ O	P ₂ O ₅	CO ₂	S	Σ	FeO ^T	Na ₂ O/Al ₂ O ₃	K ₂ O/Al ₂ O ₃
A-69.	10/2.	2,684–2,687	46.03	1.81	14.21	5.34	3.77	0.13	9.66	11.87	1.34	0.07	3.35	0.00	0.28	0.60	100.46	9.49	0.09	0.00
A-69.	10/3.	2,684–2,687	47.26	0.64	15.47	4.82	3.99	0.15	10.09	11.20	1.50	0.06	3.47	0.00	0.07	0.32	101.04	9.21	0.10	0.00
A-121.	2.	2,598–2,599	48.00	0.24	15.40	2.35	5.11	0.19	6.81	8.94	3.23	0.44	4.04	0.02	3.83	0.00	99.60	8.97	0.21	0.03

transformed to kyanite as temperature decreased (Cesare, 1999). As an alternative, kyanite may have formed due to the breakdown of staurolite along a prograde P - T path. In this case, kyanite aggregates would mimic previous staurolite porphyroblasts as pseudomorphs. Horváth and Árkai (2002) reported relict staurolite grains from a few mica schist specimens from the AH area. They suggested that kyanite was formed at the expense of staurolite at about 570–650 °C and 600–900 MPa. Since there is no textural evidence for the garnet → sillimanite → kyanite reaction sequence and the studied samples do not contain relict staurolite, the possibility of these two scenarios is ruled out.

A further alternative for the P - T conditions of the second metamorphic stage (M2), that is, replacement of garnet by kyanite, was calculated using the TWQ software in the KFLASH system (Fig. 9a). Paragenesis of the second metamorphic stage might be the result of the following reaction:

$$\text{garnet} + K - \text{feldspar} + \text{water} = \text{quartz} + \text{kyanite} + \text{biotite}$$

Considering the above reaction, the kyanite + biotite paragenesis could appear at >500 °C and >400 MPa because of a prograde hydration process.

Based on a previous study (Kendrick and Indares, 2017), one possible explanation for the replacement of garnet by fine-grained kyanite aggregates could be the crystallization of melt during retrograde metamorphism. Due to of high- P anatexis melting of aluminous rocks, the melt is mostly produced under fluid-absent conditions by the breakdown of mica. Along the prograde path, kyanite porphyroblasts are produced by muscovite dehydration melting reaction, and at even higher temperatures, biotite dehydration melting consumes these kyanite blasts. Following the metamorphic peak, new retrograde kyanite can grow as rims around the prograde kyanite porphyroblasts and as part of the groundmass or may replace garnet during melt crystallization. Based on the total absence of primary kyanite porphyroblasts in the studied samples, the retrograde formation of the kyanite aggregates is not assumed. Other research (Corey, 1960; Espenshade and Potter, 1960) emphasizes that the formation of aggregates of tiny, needle-shaped kyanite crystals is not exclusively associated with regional metamorphism in mica schists and gneisses. Instead, injection of a high Si + Al hydrothermal solution of magmatic origin may provide a suitable resource for the formation of such aggregates. In this scenario, kyanite crystals grow along with other minerals as a resulting of the circulating fluids.

Hydration reactions associated with increasing temperature, as suggested by the reaction outlined above, could be related to a contact metamorphic (metasomatic) effect caused by an igneous intrusion. During a contact metasomatic process, the high heating rate coincides with high nucleation rates and low growth rates, eventually resulting in the formation of fine-grained kyanite aggregates at the expense of garnet porphyroblasts with small biotite flakes and small-grained, second-generation garnets. The observation that both late garnet and kyanite are characterized by small grain size suggests crystallization due to a high heating

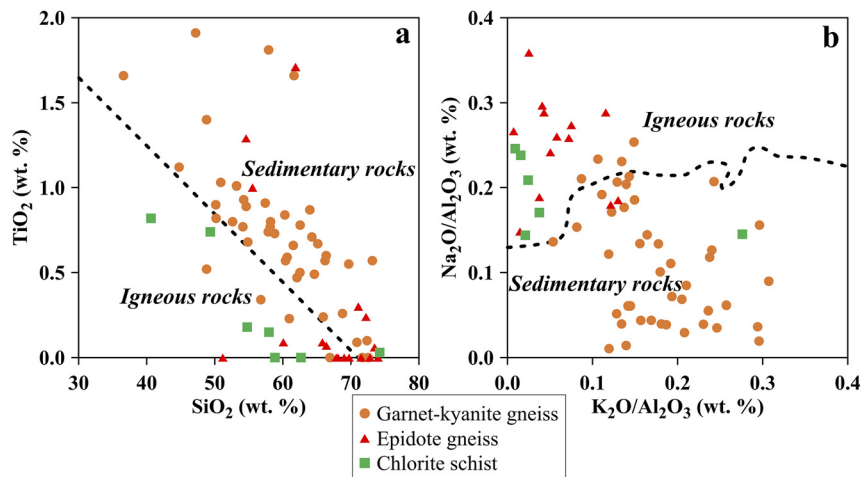


Fig. 7. (a) TiO_2 vs. SiO_2 (Shan et al., 2016) and (b) $\text{Na}_2\text{O}/\text{Al}_2\text{O}_3$ vs. $\text{K}_2\text{O}/\text{Al}_2\text{O}_3$ (Garrels and Mackenzie, 1971) discrimination diagrams applied for the photolith identification of the AH samples

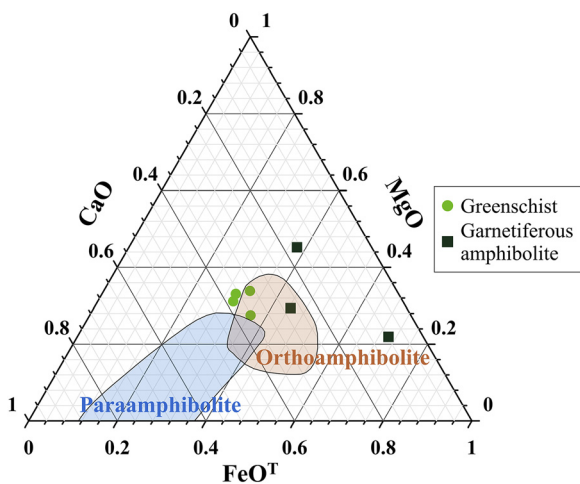


Fig. 8. Ternary diagram (Misra, 1971) used for the photolith identification of the AH samples

rate metamorphic event. Further proof for the significant role of a metasomatic activity in the studied gneisses and mica schists could be the widespread presence of post-kinematic apatite and tourmaline crystals of idiomorphic habit. This interpretation is in good agreement with previous studies. Szederkényi (1984) assumed that the schists and gneisses of the AH area were affected by contact pneumatolytic metasomatism, accompanied by positive Mo, Sn and W anomalies as well as tourmaline mineralization.

Consequently, a combination of regional metamorphism (M1) overprinted by a later contact metamorphic (metasomatic) event (M2) during decompression in the stability field of kyanite linked to an igneous intrusion is the most satisfactory explanation for the metamorphic evolution of the rock types in question. Considering this interpretation, a reliable clockwise P - T path that avoids the andalusite field could be assembled for the gneiss and mica schist.

The typical deformation features, presence of asymmetric δ -clasts, together with boudinage, mica fishes, S-C

fabrics, as well as dynamically recrystallized quartz ribbons, all indicate intensive mylonitic deformation coeval with the second deformation phase (D2), resulting in the creation of mylonitic gneiss. Chloritization, sericitization and saussurization are interpreted as results of reactions along the retrograde path.

The slightly oriented amphibole and biotite grains of the garnetiferous amphibolite define the S1 foliation plane. Peak metamorphic conditions are defined by the inclusion-rich garnet, the green or dark brown amphibole and grains of rutile. A total lack of typical greenschist facies minerals (epidote, actinolite, chlorite and titanite) and the presence of the biotite + hornblende + garnet + rutile mineral assemblage implies middle amphibolite facies conditions at ~ 600 °C was attained (Bucher and Grapes, 2011). The zonation of amphibole crystals reflects a change in chemical composition from hornblende at the core to a more actinolitic rim. This feature, together with rutile needles fringed by titanite, suggests a retrograde overprint under greenschist facies conditions.

Observation of relic myrmekitic feldspar grains, polygonal microtextured quartz-feldspar domains and the euhedral habit of accessory zircon grains, suggests the protolith of the epidote gneiss would have been an intrusive granitoid rock. Myrmekites typically occur in granitic rocks formed by igneous crystallization; however, many different genetic models are known, including solid-state exsolution models, progressive or retrograde metamorphic reaction models, metasomatic replacement models and deformation models (Zachar and M. Tóth, 2001). According to Vernon and Collins (1988), relic polygonal textures are the best distinctive indicators for orthogneisses. The euhedral habit of zircon crystals likely does not represent grains of transported, sedimentary origin; instead, they are indicative of an intrusive magmatic origin. Beside all the observed petrographic features, sample geochemical compositions confirm the magmatic origin of this rock type. In the studied gneiss samples, one foliation plane can be identified (S1), as defined

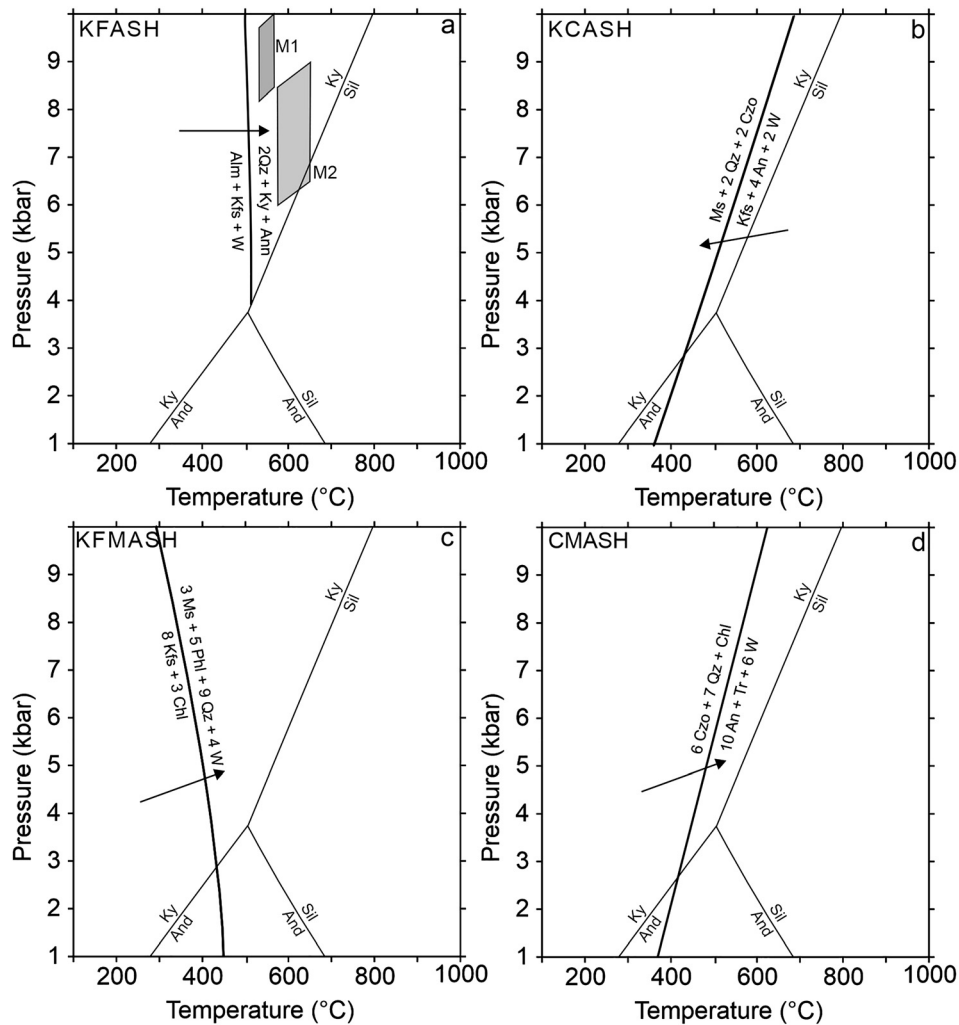
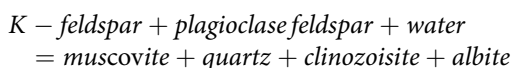


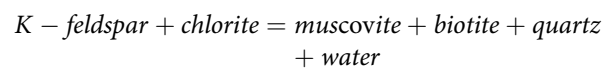
Fig. 9. Estimation of *P*–*T* conditions of (a) garnet-kyanite gneiss and mica schist; (b) epidote gneiss; (c) chlorite schist; (d) greenschist using the TWQ software. The diagrams show the relevant reactions formed the mineral assemblages. The arrows indicate segments of the hypothetical *P*–*T* paths. The chemical systems are marked on the top left side of the diagrams. The gray boxes represent the *P*–*T* conditions calculated by Horváth and Árkai (2002) for garnet-kyanite gneiss. Mineral abbreviations after Whitney and Evans (2010)

by biotite bands and muscovite flakes. Occasionally, presence of dynamically recrystallized, elongated quartz ribbons and asymmetric feldspar δ -clasts suggest coeval mylonitization. Following emplacement, the major metamorphic event affecting the granitoid protolith was retrograde under greenschist facies conditions and was accompanied by rutile crystallization results from chloritization of biotite, sericitization and formation of late epidote due to the reaction



Formation of epidote aggregates is especially typical in the wings of the asymmetric feldspar δ -clasts. Based on estimates of the *P*–*T* conditions of this reaction in the KCASH system (that is, plagioclase lacks an albite component) using the TWQ software, the retrograde reaction started at a temperature of about 400–500 °C along a decreasing *T* path (Fig. 9b).

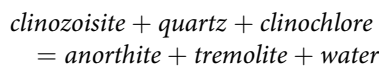
Chlorite schists display an S1 foliation plane as defined by chlorite rods and in places by biotite flakes, indicative of formation by progressive, greenschist facies metamorphism (M1). Biotite grains along chlorite rims likely developed by the following reaction:



Consequently, the peak metamorphic conditions in the KFMASH system are estimated to be in the chlorite-biotite zone at ~400 °C (Fig. 9c). Idiomorphic epidote grains along the chlorite rods, siderite aggregates, calcite lenses, rutile and undeformed, disseminated ore minerals (magnetite, pyrite and chalcopyrite) are all post-kinematic relative to S1 and are assumed to have formed by a late metasomatic process. Epidote, chlorite and carbonate (siderite) are typical products in propylitic rock alteration produced by weakly acidic to near-neutral hydrothermal fluids at 200–350 °C.

Propylitic alteration is commonly associated with the formation of ore deposits (Zharikov et al., 2007), yet in the present study, it resulted in magnetite, pyrite and chalcopyrite precipitation and hydrothermal rutile formation in the chlorite schists. Titanite replacement by rutile (\pm calcite) is also owing to the interaction of hydrothermal fluids. In some samples, the sheared, boudinaged ore mineral phases, together with fibrous calcite strain fringes around rigid pyrite crystals and crenulation cleavage suggest shearing following the metasomatic overprint due to a second deformation phase (D2). The appearance of such fibers in a fringe structure carries information about the conditions of the deformation event (Passchier and Trouw, 2005). In the case of the chlorite schists, these structures typically indicate shearing in one direction within a short time (Durney and Ramsay, 1973).

The greenschists are characterized by fine-grained chlorite, epidote and actinolite/tremolite grains that define the main foliation (S1). The presence of these phases records progressive greenschist facies conditions related to the reaction calculated by the TWQ software in the CMASH system:



for which the peak P - T conditions are estimated at around 400–500 °C with the appearance of amphibole grains (Fig. 9d). The paragenesis represents typical greenschist facies minerals in the metabasite system referring to peak conditions below the amphibolite facies.

Based on microscopic analysis, two types of tectonites were identified in the study area: fault breccia and cataclasite. The fragments of fault breccias contain highly deformed, dynamically recrystallized quartz grains and mica fishes. These textural features are related to a ductile deformation event before the brittle deformation. Consequently, the protolith of fault breccias should be the mylonitic gneiss. The clast material of the strongly fragmented cataclasite is monomineralic; therefore, its protolith cannot be identified.

Nature of the protolith

On major element discriminant diagrams, the main rock types are well-distinguished. The large scatter of values might be the result of the significant retrograde overprint and the effect of the hydrothermal/pneumatolytic processes identified in most cases.

Both SiO_2 vs. TiO_2 and $\text{K}_2\text{O}/\text{Al}_2\text{O}_3$ vs. $\text{Na}_2\text{O}/\text{Al}_2\text{O}_3$ diagrams give consistent results for the two types of gneisses and the chlorite schist (Fig. 7). On both diagrams, garnet-kyanite gneiss and mica schist data plot in the sedimentary field, whereas epidote gneiss and chlorite schist show an igneous origin. Beside their different mineralogical and textural characteristics, garnet-kyanite gneiss and epidote gneiss can be distinguished based on their chemical composition as well, in that garnet-kyanite gneiss is higher in TiO_2 , Al_2O_3 and K_2O and lower in Na_2O . Consequently,

the discriminant diagrams confirm the different protoliths of the two gneiss varieties. The values of chlorite schist fall into the igneous field on both diagrams. Similar to the epidote gneiss, it is characterized by a higher Na_2O , but lower SiO_2 content than the garnet-kyanite gneiss and mica schist. Although the chlorite schist has a similar major element composition to the epidote gneiss, the microtextural features of the two rock types are significantly different, so they should represent different rock types. The CaO - MgO - FeO^T ternary diagram revealed that most of the greenschist and garnetiferous amphibolite plot in the orthoamphibolite field (Fig. 8).

Spatial correlation of rock types

A point map of the identified rock types (Fig. 10a) suggests that all main lithologies appear clustered, so their spatial extensions could be defined as well (Fig. 10b). However, the positions of the boundaries between the distinct fields are highly hypothetical.

Garnet-kyanite gneiss and mica schist are dominant in the northwestern and southeastern parts of the crystalline dome. In these areas, garnetiferous amphibolite was observed in two boreholes. In a single borehole in the NW, both kyanite-garnet gneiss and garnetiferous amphibolite appear (Fig. 10). Using discriminant diagrams based on major element composition, these rock types have quite different protoliths, which both experienced amphibolite facies peak conditions. These two rock types consequently evolved simultaneously. Similarities in petrographic and geochemical features as well as the estimated P - T conditions indicate the NW and SE parts of the area likely represent disaggregated blocks of the same rock body.

Epidote gneiss is typically located exclusively in the central part of the area. In the adjacent boreholes, chlorite schist is found in boreholes that extend along a NW-SE-oriented zone. Greenschist could be identified in only two boreholes in the southeastern region of the AH (Fig. 10). The metamorphic histories of epidote gneiss, chlorite schist and greenschist in the central part are quite different from what is considered typical in the garnet-kyanite gneiss and garnetiferous amphibolite-dominated realm. The peak metamorphic paragenesis of these lithologies encountered in the central region may have formed at temperatures ~400–500 °C under greenschist facies conditions. However, the evolution of these three, low-grade lithologies cannot be unified either. Due to the presence of relic myrmekitic feldspar grains, polygonal microtextured quartz-feldspar domains and the euhedral habit of the accessory zircon grains, the protolith of epidote gneiss is an intrusive, granitoid rock type that was metamorphosed along a retrograde path. Conversely, chlorite schist and greenschist exhibit clear progressive metamorphic textures and so reached maximum P - T under greenschist facies conditions. On this basis, the regions dominated by these two rock types can be merged on the map in Fig. 10. Considering the significant difference in petrographic features and the metamorphic evolutions between the northwestern, the southeastern and two

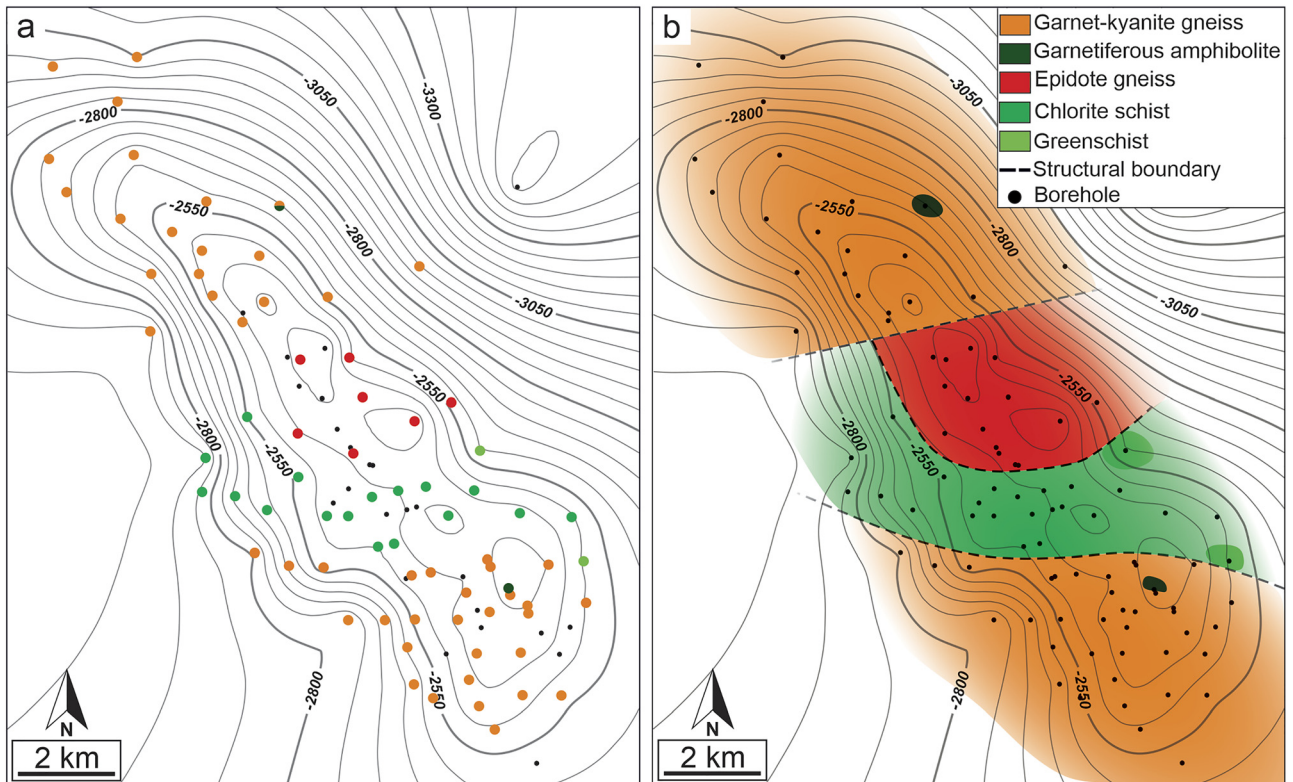


Fig. 10. Point map (a) and lithologic map (b) based on the spatial extension of data points

subsections of the central area of the AH, post-metamorphic structural boundaries have been assumed among them.

Independent evolutionary pathways of the epidote gneiss- and the chlorite schist-dominated blocks is further confirmed by the presence of the propylitic overprint in the chlorite schists but is undetected in the epidote gneiss samples. The post-kinematic textural position of magnetite, pyrite and chalcopyrite grains, as well as the calcite, epidote and siderite assemblage in most chlorite schist samples, strongly suggests that they should not represent the protolith and instead represent post-peak hydrothermal activity (Fig. 11). Since the ore mineralization is missing in the adjacent epidote gneiss samples and the two rock types have fundamentally different *P-T* paths, these two blocks had to become juxtaposed following the ore mineralization event, and so a structural boundary is assumed between them.

Although there is no seismic proof for fault zones between the above detailed lithological realms, their existence can be deduced from their significantly different metamorphic histories. Petrographically, such a fault zone must be marked by the presence of tectonic rocks. Mylonitization of all rock types is common in the entire study region (Fig. 12) and so does not seem to be related to these structural zones. The few tectonic rock specimens in the present study that formed due to brittle deformation (cataclasite and fault breccia) appear to be aligned with the presumed structural boundaries (Fig. 12). Both fault breccias and cataclasites are located in two specific zones of the area: in the northwestern region, they are located between the

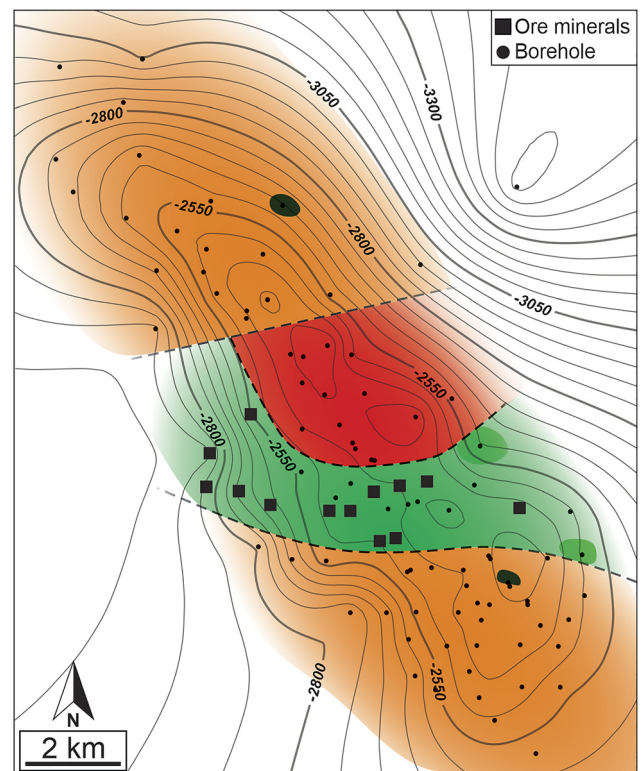


Fig. 11. Lithologic map of post-kinematic ore minerals (magnetite, pyrite and chalcopyrite) confirmed by the exploratory boreholes

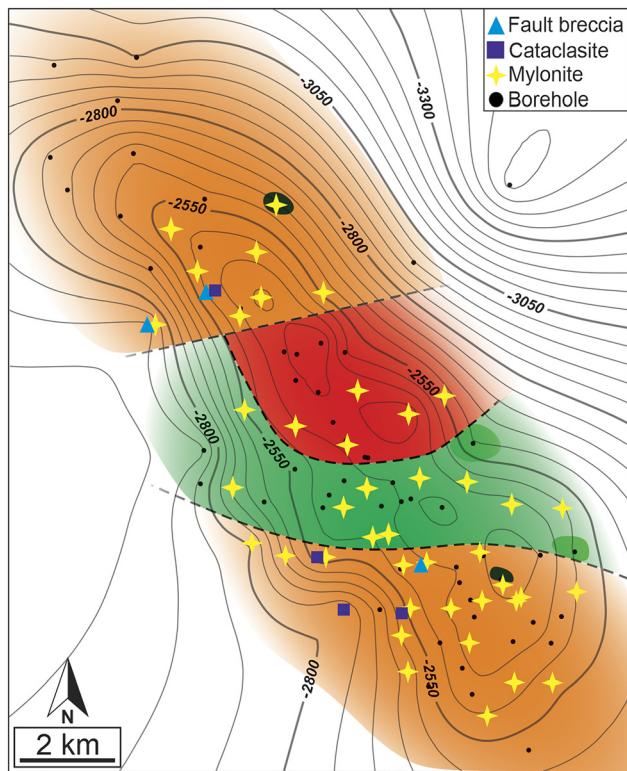


Fig. 12. Lithologic map about different tectonites confirmed by the exploratory borehole

garnet-kyanite gneiss and the epidote gneiss blocks and in the southeastern region between the garnet-kyanite gneiss and the chlorite schist blocks (Fig. 12). The fact that most fragments of the fault breccias consist of mylonitic gneiss demonstrates the occurrence of a ductile deformation event before brittle deformation.

Considering the spatial positions of the major lithologies, it is evident that the AH was constructed from blocks with different petrographic features, as well as differing metamorphic and post-metamorphic evolutions. These metamorphic blocks most probably became juxtaposed along post-metamorphic structural boundaries, which formed simultaneously with intensive brittle deformation.

Geologic interpretation

In agreement with the results of previous studies, the metamorphic mass of the AH is rather complex petrographically and contains varieties of different gneiss and mica schist, amphibolite, chlorite schist and epidote-bearing rocks as the major lithologies (Szederkényi, 1984; T. Kovács and Kurucz, 1984). T. Kovács and Kurucz (1984) suggested that these rock types appear in distinct blocks, with kyanite gneiss and mica schist typical located at the northern and southern parts of the area and chlorite schists and epidote-bearing rocks found in the central region. They also assumed the presence of hypothetical fault zones between the adjacent blocks without any structural interpretation or mapping.

The supposed contact metasomatic effect of the garnet-kyanite gneiss and mica schist is in good agreement with

previous studies. These interpretations showed that the local surroundings of the AH were affected by intrusions of granite and granodiorite ('banatite') bodies (Szalay, 1977; Szederkényi, 1984; Berza et al., 1998). Szederkényi (1984) assumed that the schists and gneisses of the AH area were affected by contact pneumatolytic metasomatism. The widespread Late Cretaceous (82–95 Ma) Ar–Ar secondary muscovite ages published by Lelkes-Felvári et al. (2003) for the area can be related to the age of this contact metamorphic overprint as opposed to a regional metamorphic event.

Petrography and petrological interpretation of the garnetiferous kyanite gneiss zone of the neighboring Dorozsma High (DH) are identical to those documented for the AH garnetiferous kyanite gneiss and mica schist blocks. Furthermore, the presence of post-kinematic muscovite and tourmaline are documented in the Dorozsma area and are interpreted as a contact metasomatic overprint caused by banatite magmatism (M. Tóth, 2008). Similarities between the petrographic features of the garnet-kyanite gneisses of the northwestern and southeastern part of the AH and the uppermost block of DH (see above) suggest that these areas evolved in a comparable manner (Fig. 13a, b).

Based on these similarities and the well-known structural build-up of the DH, it is expected that below the garnet-kyanite gneiss domain of the AH region, a thin dolomite marble cataclasite horizon and at further depth an amphibolite-dominated zone should appear at depths currently unsampled in borehole cuttings (Fig. 13a, b). Detailed mapping using petrographic and well-log data suggests that the cataclasite follows thin horizons a few tens of meters thick with an ENE dip in the DH. The significant difference between the peak metamorphic temperatures of the adjacent blocks, the fact that the high-grade garnetiferous kyanite gneiss block is above the lower-grade, amphibolite-dominated one, as well as the lowest metamorphic grade of the dolomite marble and its brittle sheared character confirm that the cataclasite horizon represents a thrust sheet inside the metamorphic basement (M. Tóth and Vargáné Tóth, 2020). In the southwestern part of the Apuseni Mountains, intensely deformed, low-grade metacarbonate sequences, comparable with Dorozsma marbles, have been documented at the contact between tectonic units of the Cretaceous nappe systems (Reiser et al., 2017a, b). The deformation and metamorphic overprint of these sequences are considered to be related to Early Cretaceous nappe stacking due to the Alpine orogeny (Reiser et al., 2017a, b). Based on the similar structural position and the metamorphic history, the thrust sheet inside the DH can be interpreted as a segment of this nappe system (M. Tóth and Vargáné Tóth, 2020).

Based on the above analysis and similarities of metamorphic events, an identical structure can be proposed for the AH. More precisely, the presence of a thrust sheet that formed because of the Early Cretaceous compressional tectonic phase and is responsible for the juxtaposition of different metamorphic blocks could be assumed below the gneissic rocks. This amalgamated metamorphic mass must

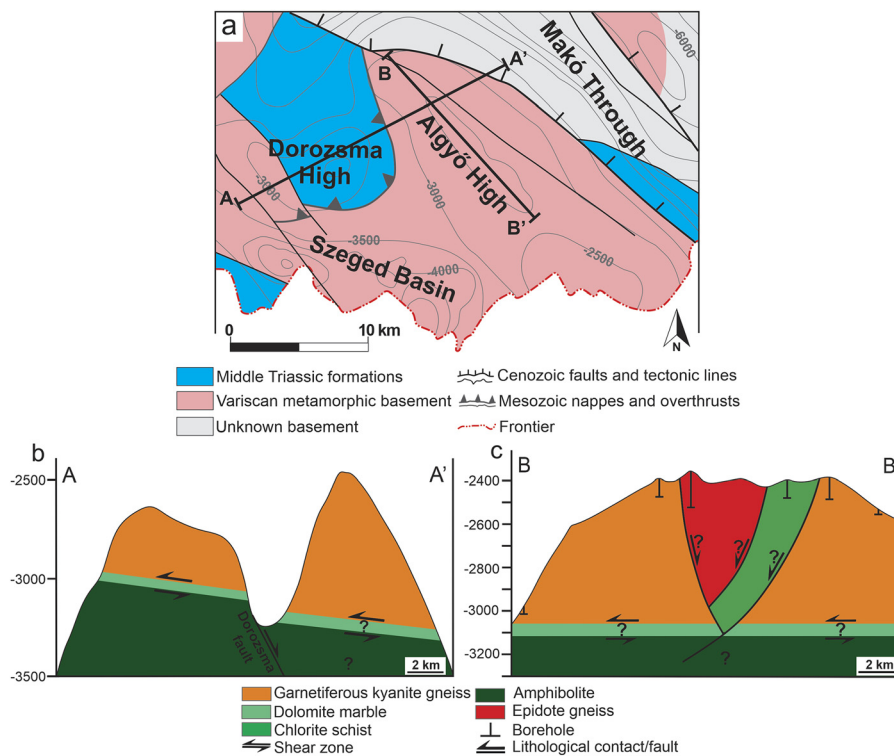


Fig. 13. Theoretical geologic sections of the studied area: (a) generalized pre-Cenozoic basement map of the studied area (modified after Haas et al., 2010); (b) cross-section across the DH and the northwestern part of AH along the line A–A'; (c) NW–SE profile of AH along the line B–B'. The Dorozsma Fault is after Tari et al. (1999)

have been affected by the contact metasomatic effect afterward. Furthermore, this post-kinematic hydrothermal overprint must be linked to younger igneous activity. The most probable igneous candidates are the widespread Late Cretaceous banatite intrusions both in the DH and the AH regions.

The petrographic features and metamorphic histories of the epidote gneiss and chlorite schist blocks of the central part of AH are significantly different from those documented for the northwestern and southeastern parts of the High. These rock types are essentially unknown from the surrounding crystalline basement in the southeastern part of Hungary. Since the propylitic overprint and ore mineralization of the chlorite schist are missing in the adjacent epidote gneiss and the two rock types have essentially different metamorphic histories, they should represent two different blocks separated by post-metamorphic and post-hydrothermal structures. Furthermore, the propylitic metasomatic overprint of the chlorite schist block resulted in quite different mineralization from the contact pneumatolytic metasomatism of the garnet-kyanite gneiss, although no details of the physicochemical circumstances of these two post-metamorphic events are known yet. If the metasomatic overprint in both blocks can be linked to the banatite intrusions, they should have been located at different positions relative to the intrusions so that they could represent diverse portions of the pre-existing lithosphere. As the nappe movements discussed above are Early Cretaceous in age, this compressional tectonic event could not have been

responsible for the juxtaposition of the different metamorphic blocks inside the AH. The zones that separate the two garnetiferous kyanite gneiss blocks from the epidote gneiss and the chlorite schist blocks, as well as those that separate the two further realms from each other, must be even younger.

Syn-rift extension in the Middle Miocene caused the development of numerous low-angle normal fault systems resulting in metamorphic core complex formation in the metamorphic basement of the Pannonian Basin (Tari et al., 1992; Tari, 1996). Geophysical interpretations (Rumpler and Horváth, 1988; Posgay et al., 1996; Tari et al. 1999) showed that the AH has a metamorphic core complex structure formed by this process. The presence of the Miocene core complex is also suggested by Middle Miocene 17 ± 0.8 Ma zircon fission-track ages from the AH (Tari et al., 1999). The different metamorphic blocks of the northwestern, southeastern and the central part of AH most probably became juxtaposed along post-metamorphic normal fault boundaries developed due to this Miocene extensional event (Fig. 13a, c). Further details about the character and the exact position of these normal fault systems can be evaluated only using seismic data and so are not within the scope of this paper.

Formation of the major structure of the AH due to Miocene extension was followed by post-rift inversion and basin subsidence since the Middle Miocene (Tari et al., 1999). During the Neogene, the Paleozoic metamorphic highs and the adjacent deep basins became covered by thick

sediments (Horváth and Tari, 1999). These Neogene sedimentary sequences overlying the basement highs have the best hydrocarbon reservoir characteristics in the south-eastern part of Hungary. Additionally, the brittle fault zones and the fractured hard rock bodies of the basement highs play an important role in hydrocarbon migration and the accumulation (M Tóth, 2008; M Tóth et al., 2007; M Tóth and Vargáne Tóth, 2020; Molnár et al., 2015; Nagy et al., 2013; Schubert et al., 2007; Vass et al., 2018). The results of the present study prove that the metamorphic mass of the AH may also be an essential part of the local hydrocarbon system. The probable post-metamorphic, brittle structural boundaries between the huge blocks with different metamorphic and post-metamorphic evolutions could provide hydrocarbon migration pathways from the adjacent over-pressured sub-basins (Szeged Basin, Makó Trough) or could even provide reservoir characteristics.

CONCLUSION

The lithological character and geologic evolution of the AH area were investigated based on the comprehensive petrologic study in conjunction with the analysis of the spatial position of the major lithologies.

The northwestern and southeastern part of the area is characterized by garnet-kyanite gneiss and mica schist of sedimentary origin and garnetiferous amphibolite of igneous origin. The first amphibolite facies regional metamorphism of the gneiss and mica schist was overprinted by a contact metamorphic (metasomatic) effect in the stability field of kyanite during decompression. This event was accompanied by the formation of fine-grained kyanite aggregates and a second generation of small-grained garnet. Contact metasomatism also resulted in the formation of idiomorphic tourmaline, apatite crystals and epidote aggregates. Garnetiferous amphibolite experienced amphibolite facies peak conditions comparable with the host gneiss. Regarding the similarities in petrologic features, the northwestern and southeastern parts of the AH represent disaggregated blocks of the same rock body.

The central part of the area is characterized by an epidote gneiss-dominated block and a chlorite schist-dominated block. The metamorphic histories of these lithologies are quite different from those characterizing the northwestern and southeastern regions; however, the evolution of these two blocks cannot be unified either. The protolith of epidote gneiss is an intrusive, granitoid rock type, possibly metamorphosed along with a greenschist facies retrograde pathway.

By contrast, chlorite schist reveals clear greenschist facies progressive metamorphic features. The independent evolution of these two blocks is further confirmed by the presence of a prophyllitic overprint in chlorite schist.

The results of the present study suggest that the AH was constructed from blocks with different petrographic features and metamorphic histories; therefore, structural boundaries

are assumed to exist between them. These metamorphic blocks most probably became juxtaposed along normal faults simultaneously with intensive brittle deformation during extensional processes coeval with the opening of the Pannonian Basin during the Miocene. The supposed brittle structural boundaries between the blocks could provide hydrocarbon migration pathways from the adjacent over-pressured sub-basins or could even represent suitable reservoirs.

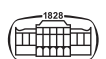
ACKNOWLEDGEMENTS

The MOL Hungarian Oil and Gas Company is thanked for providing thin sections and core samples for investigation. The authors thank Enago from Crimson Interactive Pvt. Ltd. for the English language editing.

REFERENCES

- Babinszki, E. and Kovács, Zs. (2018). Hydrocarbon exploration areas in Hungary – Szeged Basin and the Kiskunság. In: Kovács Zs. (Ed.), *Hydrocarbons in Hungary*, Budapest, pp. 83–105.
- Balogh, K. and Pécskay, Z. (2001). K/Ar and Ar/Ar geochronological studies in the PANCARDI region. *Acta Geologica Hungarica*, 44(2.3): 281–299.
- Berman, R. G. (1991). Thermobarometry using multi-equilibrium calculations: a new technique, with petrological applications. *Canadian Mineralogist*, 29: 833–855.
- Berza, T., Constantinescu, E., and Vlad, S. (1998). Upper Cretaceous magmatic series and associated mineralization in the Carpathian-Balkan orogen. *Resource Geology*, 48: 291–306.
- Bucher, K. and Grapes, R. (2011). *Petrogenesis of metamorphic rocks*. Springer Berlin Heidelberg, pp. 269–277.
- Cesare, B. (1999). Multi-Stage pseudomorphic replacement of garnet during polymetamorphism: 1. Microstructures and their interpretation. *Journal of Metamorphic Geology*, 17: 735–746.
- Corey, A. F. (1960). Kyanite occurrences in the Petaca District, Rio Arriba County, New Mexico. – State Bureau of Mines and Mineral Resources, New Mexico Institute of Mining and Technology, *Bulletin*, 47: 40–53.
- Csontos, L., Nagymarosy, A., Horváth, F., and Kováč, M. (1992). Cenozoic evolution of the Intra-Carpathian area: a model. *Tectonophysics*, 208(1–3): 221–241.
- Csontos, L. and Vörös, A. (2004). Mesozoic plate tectonic reconstruction of the Carpathian region. *Palaeogeography, Palaeoclimatology, Palaeoecology*, 210: 1–56.
- Dimitrescu, R. (1995). Contributii la corelare unităților de fundamentale Munților Apuseni și Carpaților Meridionali cu cele din depresiunea pannonică și de peste dunăre. *St. Cerc. Geologie*, 40: 133–139.
- Dolton, G. L. (2006). Pannonian Basin Province, Central Europe (Province 4808) - Petroleum geology, total petroleum systems, and petroleum resource assessment. U.S. Geological Survey Bulletin 2204-B, pp. 23.

- Durney, D. W. and Ramsay, J. G. (1973). Incremental strains measured by syntectonic crystal growths. In: DeJong, K. A. and Scholten, R. (Eds.), *Gravity and tectonics*. Wiley, New York, pp. 67–95.
- Espenshade, G. P. and Potter, D. B. (1960). Kyanite, Sillimanite, and Andalusite Deposits of the Southeastern States. *U.S. Geological Survey Professional Paper*, 336: 19–27.
- Fodor, L., Csontos, L., Bada, G., Györfi, I., and Benkovics, L. (1999). Tertiary tectonic evolution of the Pannonian Basin system and neighbouring orogens: a new synthesis of paleostress data. In: Durand, B., Jolivet, L., Horváth, F., and Seranne, M. (Eds.), *The mediterranean basins: Tertiary extension within the Alpine orogene*, Vol. 156. Geological Society, London, Special Publication, pp. 295–334.
- Garrels, R. M. and McKenzie, F. T. (1971). *Evolution of sedimentary rocks*. W.W. Norton and Co. Inc. New York. pp. 394.
- Haas, J. (2001). *Geology of Hungary*. Eötvös University Press, Budapest.
- Haas, J., Budai, T., Csontos, L., Fodor, L., and Konrád, Gy. (2010). *Pre-Cenozoic geological map of Hungary 1:500 000*. Hungarian Geological Institute.
- Horváth, F. and Tari, G. (1999). IBS Pannonian Basin project; a review of the main results and their bearings on hydrocarbon exploration. In: Durand, B., Jolivet, L., Horváth, F., and Seranne, M. (Eds.), *The mediterranean basins: Tertiary extension within the Alpine orogene*, Vol. 156. Geological Society, London, Special Publication, pp. 195–213.
- Horváth, P. and Árkai, P. (2002). Pressure-temperature path of metapelites from the Algyó-Ferencszállás area, SE Hungary: thermobarometric constraints from coexisting mineral assemblages and garnet zoning. *Acta Geologica Hungarica*, 45(1): 1–27.
- Kendrick, J. and Indares, A. (2017). The reaction history of kyanite in high-pressure aluminous granulites. *Journal of Metamorphic Geology*, 36: 125–146.
- Lelkes-Felvári, Gy., Frank, W., and Schuster, R. (2003). Geochronological constraints of the Variscan, Permian-Triassic and eo-Alpine (Cretaceous) evolution of the Great Hungarian Plain basement. *Geologica Carpathica*, 54: 267–280.
- Lelkes-Felvári, G., Schuster, R., Frank, W., and Sassi, R. (2005). Metamorphic history of the Algyó High (Tisza Mega-unit, basement of Great Hungarian Plain) – a counterpart of crystalline units of the Koralpe-Wolz nappe system (Austroalpine, Eastern Alps). *Acta Geologica Hungarica*, 48: 371–394.
- M Tóth, T. (2008). *Repedezett, metamorf fluidumtarolok az Alföld aljzataban*. D.Sc. Thesis (in Hungarian).
- M Tóth, T. and Vargáne Tóth, I. (2020). Lithologically controlled behaviour of the Dorozsma metamorphic hydrocarbon reservoir (Pannonian Basin, SE Hungary). *Journal of Petroleum Science and Engineering*, 195.
- M. Tóth, T., Vass, I., Szanyi, J., and Kovács, B. (2007). Water and heat flow through uplifted metamorphic highs in the basement of the Pannonian Basin. XXXV. IAH Congress, Lisbon, Groundwater and Ecosystems, Proceedings, pp. 1–10.
- Matenco, L., and Radivojevic, D. (2012). On the formation and evolution of the Pannonian Basin: constraints derived from the structure of the junction area between the Carpathians and Dinarides. *Tectonics*, 31.
- Misra, S. N. (1971). Chemical distinction of high-grade ortho- and para-metabasites. *Norsk Geologisk. Tidsskrift*, 51: 311–316.
- Molnár, L., M. Tóth, T., and Schubert, F. (2015). Structural controls on the petroleum migration and entrapment within faulted basement blocks of the Szeghalom Dome (Pannonian Basin, SE Hungary). *Geologia Croatica*, 68(3): 247–259.
- Nagy, A., M. Tóth, T., Vásárhelyi, B., and Földes, T. (2013). Integrated core study of a fractured metamorphic HC-reservoir; Kiskunhalas-NE, Pannonian Basin. *Acta Geodaetica et Geophysical*, 48(1): 53–75.
- Neubauer, F. (2002). Contrasting Late Cretaceous to Neogene ore provinces in the Alpine-Balkan-Carpathian-Dinaride collision belt. In: Blundell, D. J., Neubauer, F., and von Quadt, A. (Eds.), *The timing and location of major ore deposits in an evolving orogen*, Vol. 204. Geological Society, London, Special publications, pp. 81–202.
- Passchier, C. W. and Trouw, R. A. J. (2005). *Microtectonics*. Springer-Verlag, Berlin, pp. 175–183.
- Posgay, K., Takács, E., Szalai, I., Bodoky, T., Hegedűs, E., Janvarine, K. I., Timár, Z., Varga, G., Bérczi, I., and Szalay, Á. (1996). International deep reflection survey along the Hungarian Geotraverse. *Geophysical Transactions*, 40(1–2): 1–44.
- Reiser, M. K., Schuster, R., Spikings, R., Tropper, P., and Fugenschuh, B. (2017a). From nappe stacking to exhumation: Cretaceous tectonics in the Apuseni Mountains (Romania). *International Journal of Earth Sciences*, 106: 659–685.
- Reiser, M. K., Schuster, R., Tropper, P., and Fugenschuh, B. (2017b). Constraints on the depositional and tectonometamorphic evolution of marbles from the Biharia Nappe System (Apuseni Mountains, Romania). *Geologica Carpathica*, 68(2): 147–164.
- Rumpler, J., and Horváth, F. (1988). Some representative seismic reflection lines from the Pannonian basin and their structural interpretation. In: Royden, L. H., and Horváth, F. (Eds.), *The Pannonian basin – a study in basin evolution*, Vol. 45. AAPG. Memoir, pp. 53–169.
- Schmid, S. M., Bernoulli, D., Fugenschuh, B., Matenco, L., Schefer, S., Schuster, R., Tischler, M., and Ustaszewski, K. (2008). The Alpine-Carpathian-Dinaridic orogenic system: correlation and evolution of tectonic units. *Swiss Journal of Geosciences*, 101: 139–183.
- Schmid, S. M., Fugenschuh, B., Kounov, A., Matenco, L., Nievergelt, P., Oberhansli, R., Pleuger, J., Schefer, S., Schuster, R., Tomljenovic, B., Ustaszewski, K., and van Hinsbergen, D. J. J. (2019). Tectonic units of the Alpine collision zone between Eastern Alps and western Turkey. *Gondwana Research*, 78: 308–374.
- Schubert, F., Diamond, L. W., and M. Tóth, T. (2007). Fluid-inclusion evidence of petroleum migration through a buried metamorphic dome in the Pannonian Basin, Hungary. *Chemical Geology*, 244: 357–381.
- Shan, H. X., Zhai, M. G., Zhu, X. Y., Santosh, M., Hong, T., and Ge, S. H. (2016). Zircon U-Pb and Lu-Hf isotopic and geochemical constraints on the origin of the paragneisses from the Jiaobei terrane, North China Craton. *Journal of Asian Earth Sciences*, 115: 214–227.
- Szalay, Á. (1977). Metamorphic-granitogenic rocks of the basement complex of the Great Hungarian Plain, Eastern Hungary. *Acta Mineralogica-Petrographica*, 23(1): 49–69.



- Szederkényi, T. (1984). Az Alföld krisályos aljzata es földtani kapcsolatai. D.Sc. Thesis, (in Hungarian).
- Szederkényi, T. (1991). Az Alföld mezozoikum előtti képződményeinek komplex földtani-kőzettani-geokémiai vizsgálata II., internal report. *Library of Department of Mineralogy, Geochemistry and Petrology, University of Szeged* (in Hungarian).
- T. Kovács, G., and Kurucz, B. (1984). A Dél-Alföld mezozoikumnál idősebb képződményei. In: *A Magyar Állami Földtani Intézet alkalmi kiadványa*, Budapest, pp. 15–19.
- Tari, G. (1996). Extreme crustal extension in the Raba River extensional corridor (Austria/Hungary). *Gesellschaft der Geologie- und Bergbaustudenten in Österreich*, 41: 1–17.
- Tari, G., Horváth, F., and Rumpler, J. (1992). Styles of extension in the Pannonian Basin. *Tectonophysics*, 208: 203–219.
- Tari, G., Dövényi, P., Dunkl, I., Horváth, F., Lenkey, L., Ștefănescu, M., Szafián, P., and Tóth, T. (1999). Lithospheric structure of the Pannonian Basin derived from seismic, gravity and geothermal data. In: Durand, B., Jolivet, L., Horváth, F., and Seranne, M. (Eds.), *The mediterranean basins: Tertiary extension within the Alpine orogene*, Vol. 156. Geological Society, London, Special Publication, pp. 215 – 250.
- Vass, I., M. Tóth, T., Szanyi, J., and Kovács, B. (2018). Hybrid numerical modelling of fluid and heat transport between the overpressured and gravitational flow systems of the Pannonian Basin. *Geothermics*, 72: 268–276.
- Vernon, R. H., and Collins, W. J. (1988). Igneous microstructures in migmatites. *Geology*, 16: 1126–1129.
- Whitney, D. L., and Evans, B. W. (2010). Abbreviations for names of rock-forming minerals. *American Mineralogist*, 95: 185–187.
- Zachar, J., and M. Tóth, T. (2001). Myrmekite-bearing gneiss from the Szeghalom Dome (Pannonian Basin, SE Hungary). Part II.: Myrmekite formation theories. *Acta Mineralogica-Petrographica*, 42: 39–43.
- Zharikov, V. A., Pertsev, N. N., Rusinov, V. L., Callegari, E., and Fettes, D. J. (2007). Metasomatism and metasomatic rocks. In: *A classification of metamorphic rocks and Glossary of Terms. Recommendations by the IUGS Subcommittee on the Systematics of metamorphic rocks: Web version 01. 02. 07.*

